

LLE Review

Quarterly Report



July–September 1986

UR
LLE

Laboratory for Laser Energetics
College of Engineering and Applied Science
University of Rochester
250 East River Road
Rochester, New York 14623-1299

LLE Review

Quarterly Report

Editor: B. Yaakobi
(716) 275-4926

July–September 1986



Laboratory for Laser Energetics
College of Engineering and Applied Science
University of Rochester
250 East River Road
Rochester, New York 14623-1299

This report was prepared as an account of work conducted by the Laboratory for Laser Energetics and sponsored by Empire State Electric Energy Research Corporation, General Electric Company, New York State Energy Research and Development Authority, Ontario Hydro, Southern California Edison Company, the University of Rochester, the U.S. Department of Energy, and other United States government agencies.

Neither the above named sponsors, nor any of their employees, makes any warranty, expressed or implied, or assumes any legal liability or responsibility for the accuracy, completeness, or usefulness of any information, apparatus, product, or process disclosed, or represents that its use would not infringe privately owned rights.

Reference herein to any specific commercial product, process, or service by trade name, mark, manufacturer, or otherwise, does not necessarily constitute or imply its endorsement, recommendation, or favoring by the United States Government or any agency thereof or any other sponsor.

Results reported in the LLE Review should not be taken as necessarily final results as they represent active research. The views and opinions of authors expressed herein do not necessarily state or reflect those of any of the above sponsoring entities.

IN BRIEF

This volume of the LLE Review, covering the period July–September 1986, contains reports on GDL and OMEGA laser activities; generation of timing fiducials on x-ray streak cameras on OMEGA; new theoretical results on the thermodynamic properties of high-density plasmas; experimental results and analysis of target implosions on OMEGA; calculation of thermal self-focusing with multiple laser beams; and test results of multiple x-ray diffraction in crystals. Two reports describe developments in advanced technology: subpicosecond signal propagation on superconducting transmission lines, and progress in two-dimensional image processing capabilities. Finally, the National Laser Users Facility activities for this period are summarized.

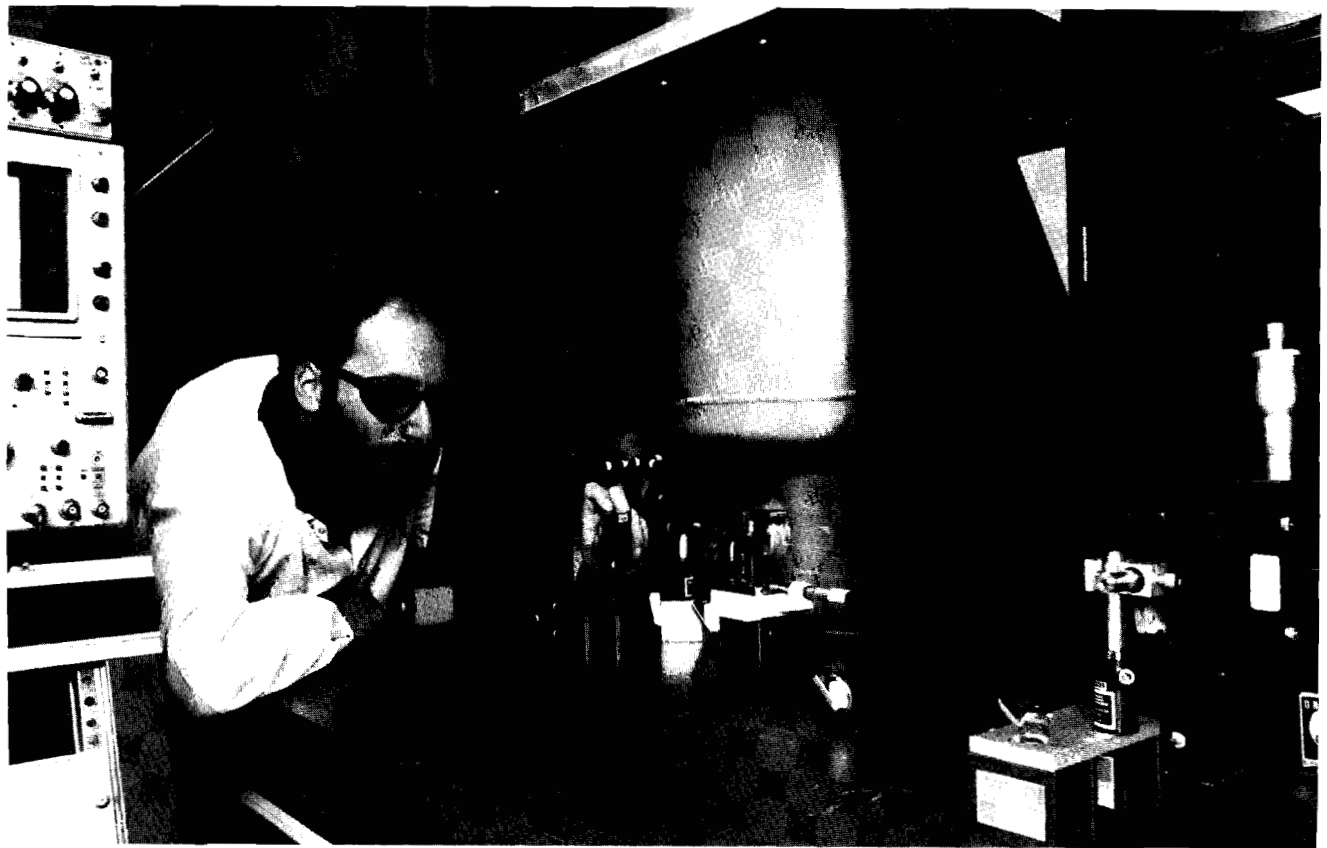
The following are some of the highlights of the research reports contained in this issue:

- Timing fiducials on OMEGA now make it possible to relate in time the measured laser pulse and streaked x-ray spectra.
- The convergence history of OMEGA-imploded shell targets closely follows the theoretical predictions. Deviations from predictions of the core emission of x rays and thermonuclear reaction products are clearly attributed to imperfect uniformity of laser irradiation.
- Two-dimensional monochromatic imaging with spatial resolution of about 10 μm has been demonstrated, using double diffraction of x rays in crystals.

- An electro-optic sampling system was used to study pulse propagation on superconducting transmission lines, where a rise time of 360 fs was measured. Dispersion broadened this time to only 2 ps after 3 mm of propagation.

CONTENTS

	<i>Page</i>
IN BRIEF	iii
CONTENTS	v
Section 1 LASER SYSTEM REPORT	141
1.A GDL Facility Report	141
1.B OMEGA Facility Report	141
Section 2 PROGRESS IN LASER FUSION	144
2.A Optical Fiducials for X-Ray Streak Cameras	144
2.B Thermodynamics of a Polarizable One-Component Plasma	149
2.C Laser-Fusion-Target Implosion Studies with OMEGA ..	155
2.D Thermal Self-Focusing with Multiple Laser Beams ..	164
2.E Multiple X-Ray Diffraction in Crystals: Application to Two-Dimensional Imaging and Low-Loss Transmission	171
Section 3 ADVANCED TECHNOLOGY DEVELOPMENTS	180
3.A Propagation of Femtosecond Electrical Pulses on Superconducting Transmission Lines	180
3.B The Image Analysis Laboratory Facility for Processing Film Data	186
Section 4 NATIONAL LASER USERS FACILITY NEWS	195
PUBLICATIONS AND CONFERENCE PRESENTATIONS	



Optical alignment of the femtosecond cryogenic sampling system is fine tuned by Douglas Dykaar, a graduate student in electrical engineering and a member of the Ultrafast Optical Electronics Center. The system is used to study ultrafast cryogenic electronics.

Section 1

LASER SYSTEM REPORT

1.A GDL Facility Report

The glass development laser (GDL) facility was used during this quarter for target experiments and has undergone further study and improvement. Focus scans and conversion-cell tuning have been completed, and damaged optics replaced. The thermal properties of the active mirrors were investigated off-line, after which they were incorporated back into the system in the double-pass configuration. Shearing tests on the second harmonic beam showed little or no defocus as a result of thermal deflection of the mirrors. Target experiments included focusing-lens characterization, diagnostic instruments activation, and experiments on x-ray radiography of targets for the Target Fabrication Group.

A summary of GDL shots during this quarter follows:

Beamline Test and Calibration Shots	119
Alignment Shots	129
Target Shots	80
TOTAL	328

1.B OMEGA Facility Report

During the fourth quarter of FY86 the OMEGA laser has undergone a number of upgrades. The driver line has been improved to provide a more uniform beam profile. This included the introduction of free

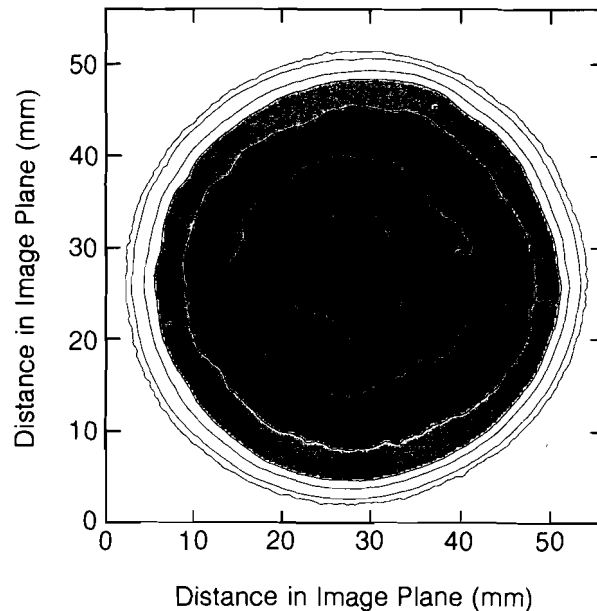
propagation of the oscillator beam over a distance of 4 m, and the addition of new diagnostics, such as a CID camera for pointing and centering verification.

A number of optical elements in the laser system were replaced to improve beam uniformity. These include several spatial filter lenses, wave plates, frequency-conversion cells, and transport optics. Linear polarizers were replaced with liquid-crystal circular polarizers, which will provide circular polarization through the red amplifiers and reject any light of birefringence-induced depolarization.

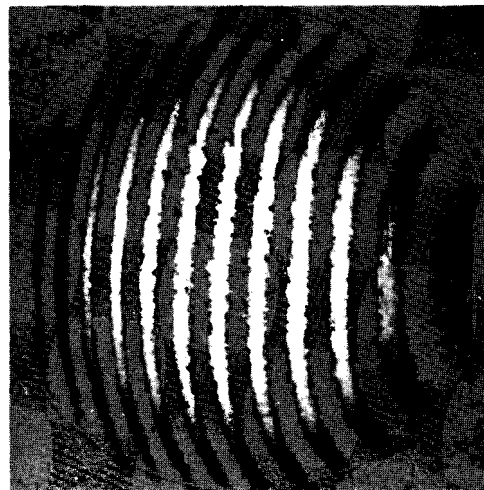
We have selected one of the beamlines (labeled 6-2) for an extensive investigation of uniformity. A corridor is being constructed around it to minimize air turbulence and thermal gradients.

Figure 28.1 demonstrates the result of the driver-line upgrade. This figure is the digitized near-field photograph of the driver output beam and shows a high degree of uniformity and circular symmetry. The degree of uniformity has been determined using an interferometer applied to the output of the driver line, and the results are shown in Fig. 28.2. The interferogram indicates total aberration of less than 1/8 of a wave. This level of performance is required to achieve the uniformity specifications of the high-density target experiments.

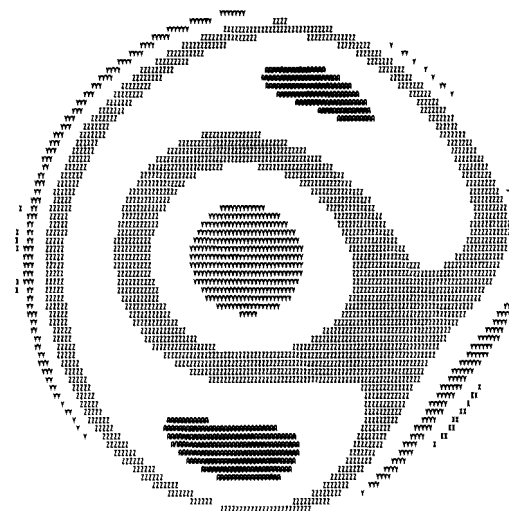
The fall series of target experiments were under way toward the end of the quarter.



*Fig 28.1
Digitized near-field photograph of driver output beam.*



interference pattern
(image enhanced)



reduced phase profile
($\lambda/5$ contour interval)

G1896

*Fig. 28.2
Interferometric representation of driver output beam.*

ACKNOWLEDGMENT

This work was supported by the U.S. Department of Energy Office of Inertial Fusion under agreement No. DE-FC08-85DP40200 and by the Laser Fusion Feasibility Project at the Laboratory for Laser Energetics, which has the following sponsors: Empire State Electric Energy Research Corporation, General Electric Company, New York State Energy Research and Development Authority, Ontario Hydro, Southern California Edison Company, and the University of Rochester. Such support does not imply endorsement of the content by any of the above parties.

Section 2

PROGRESS IN LASER FUSION

2.A Optical Fiducials for X-Ray Streak Cameras

X-ray streak cameras are the primary instruments for studying the transient nature of laser-produced plasmas. However, in order to interpret the streak record correctly and to make meaningful comparisons with numerical code simulations of the experiments, it is necessary to precisely and unambiguously relate the time of the x-ray emission to the incident laser pulse.

A variety of techniques has been used to establish a timing fiducial for the x-ray emission. An x-ray fiducial can be obtained by coating the target with a thin layer of high-Z material whose characteristic x-ray emission is discriminated spectroscopically.¹⁻³ The drawbacks of this technique are that the presence of the high-Z layer can alter the laser-plasma interaction significantly and that the timing of the onset of the x-ray emission relative to the laser pulse is not well defined. An alternative is to use a secondary laser pulse of short duration to generate a plasma off an auxiliary target that consists of a different-Z material.⁴ The relative timing of the two laser pulses can be measured using an optical streak camera, and again, the x-ray signals are discriminated spectroscopically.

A simple yet noninvasive method for obtaining a timing reference for the streak record is to use an optical fiducial.⁵ This requires, of course, the incorporation of a bifurcated photocathode into the x-ray streak camera, one section optimized for x-ray sensitivity, the other for the optical or UV spectral region. Two methods are used for generating the optical reference signals for the time-resolving x-ray diagnostics on the

24-beam OMEGA UV laser facility at LLE. First, the fraction of the incident laser light (at 351 nm) that is scattered or refracted by the plasma is used to provide a direct timing fiducial. The second method involves the frequency conversion of a small fraction of the laser driver energy to the UV ($4\omega_0$ at 264 nm). This signal is then transported via an optical fiber through the vacuum wall to the streak camera photocathode. The absolute synchronization of this signal is obtained by timing it against the scattered light signal. The latter method of providing fiducials is useful for x-ray streak camera diagnostics, which are not amenable to viewing the scattered 351-nm laser light directly.

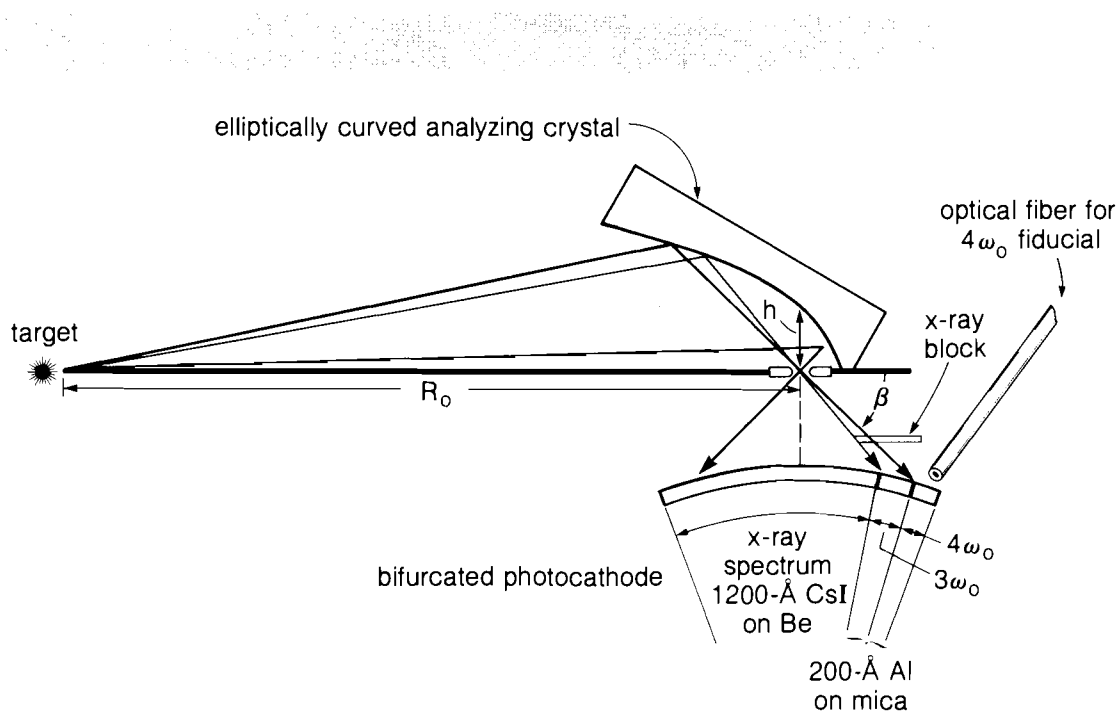
The precision in timing the optical fiducials using either of the above methods depends on how well the scattered light signal represents the actual incident laser pulse. The most precise synchronization is achieved by using a mirror, in place of the plasma, to reflect the incident laser light to the streak camera. An additional benefit from recording the light scattered from the plasma is the insight it provides on time-resolved laser absorption.

Experimental Setup

Optical fiducials are now routinely recorded on all the time-resolved x-ray spectra obtained with the streak, photographic elliptical analyzer x-ray spectrometer (SPEAXS) instrument.^{6,7} In Fig. 28.3 we present a schematic of this system. With the laser-produced "point" plasma source at one focal point of the ellipse, both the x-ray signal, which is Bragg reflected, and the incident laser light (at 351 nm), which is scattered from the plasma and reflected by the x-ray analyzer crystal, pass

Fig. 28.3

Schematic of the geometry of the streaking elliptical analyzer x-ray spectrograph with the optical fiducial signals incident on a bifurcated streak camera photocathode. The ellipse is characterized by $R_o = 120$ cm and $h = 5.08$ cm.

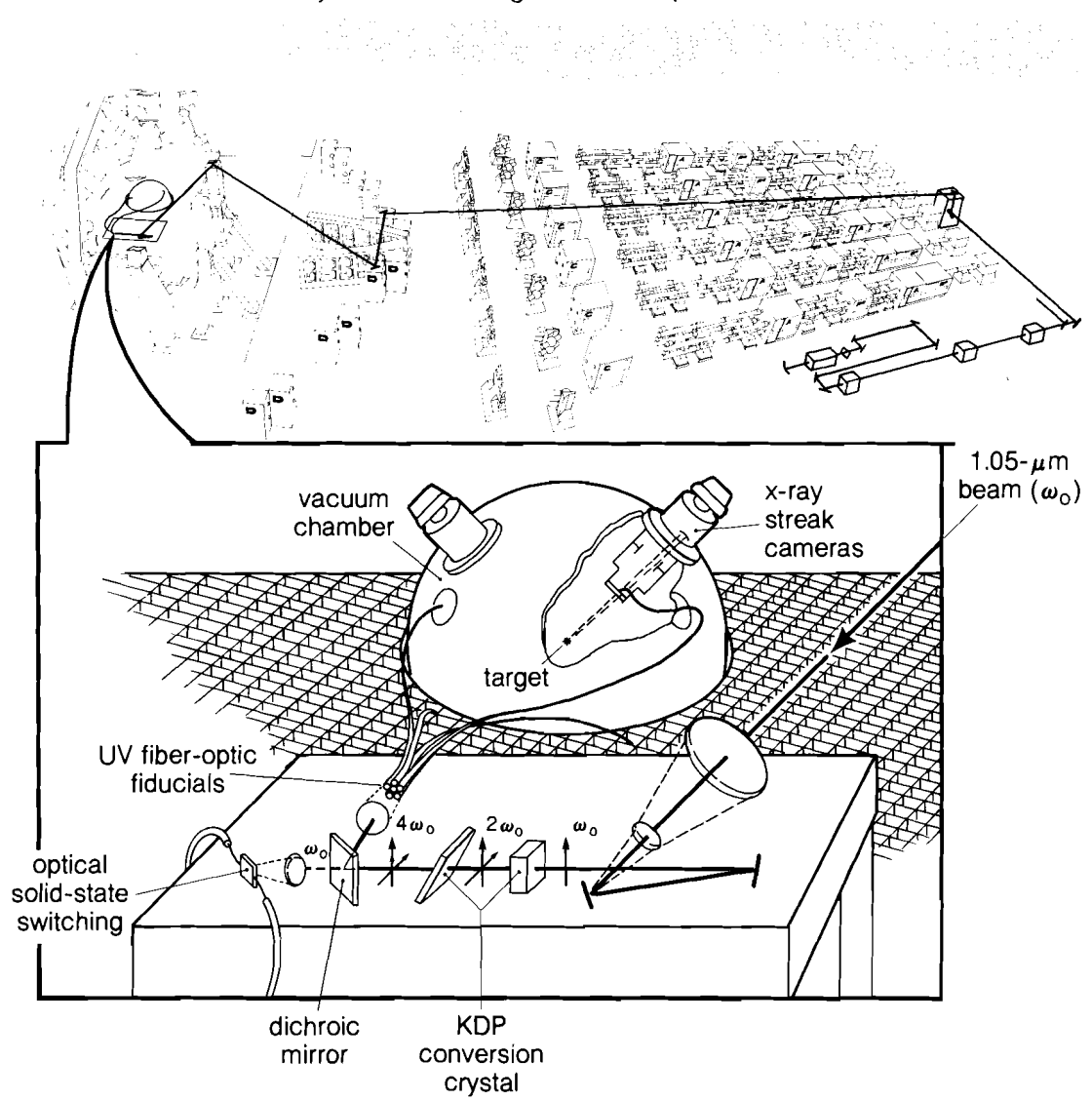


E3950

through the second focal point with no time dispersion across the spectrum. The bifurcated photocathode is located 4.4 cm from this second focal point. The time dispersion introduced by optical path differences in this section and by streak curvature in the streak tube itself, amounts to less than 50 ps and is corrected for in the data reduction. The streak camera photocathode dimensions are 1 mm by 45 mm; a section 8-mm long is used for the optical fiducials. The scattered UV-radiation signal from the target onto this section is enhanced by evaporating a 100-Å-thick layer of aluminum onto the x-ray analyzer crystal, thereby increasing its UV reflectivity.

Fig. 28.4
Schematic for producing a $4\omega_0$ (264-nm) optical fiducial on the OMEGA laser facility.

The second optical fiducial on the streak records is the $4\omega_0$ signal at 264 nm. This is derived from the OMEGA driver line and is fed into an array of quartz fibers for distribution to various streak cameras, as shown in Fig. 28.4. The optical fibers have a core diameter of 400 μm



E3410

and are typically 6.5-m long, with a transmission at 264 nm of 75% per meter. The multimode dispersion in these fibers is insignificant for the 400-ps to 600-ps pulses we use.

The x-ray-sensitive material of the transmission-mode photocathode that is commonly used is 1200-Å CsI on a 12.7- μm Be substrate. For x rays with energies less than 1 keV, a 250-Å Au photocathode on a 2000-Å parylene substrate is used. The secondary electron yields for both of these x-ray photocathodes are well known.⁸ The transmission-mode photocathode for the optical fiducials consists of 200 Å of aluminum on a mica substrate. Aluminum has been found to be the most sensitive photoemissive material for 351-nm irradiation.^{9,10} Very thin layers of mica with a measured transmission exceeding 33% at 264 nm provide a simple, yet rugged substrate for the UV photocathode. These photocathode materials are stable and can withstand the occasional exposure to the ambient atmosphere.

Experimental Results

The streak record from a 583- μm -diameter glass microballoon target shot, as obtained by the SPEAXS instrument, is presented in Fig. 28.5. An overlay of the corresponding time lineouts of the x-ray signal (2.3 to 2.45 keV) and the optical fiducial signals are shown in Fig. 28.6. In general, the scattered $3\omega_0$ signal will be shorter in duration than the incident laser pulse, but it does give an indication of the time-resolved laser absorption. Specifically, the second peak in the scattered $3\omega_0$ signal at 1.85 ns is attributed to an increase in refraction as the critical surface moves inward during the implosion. The peak in the x-ray signal

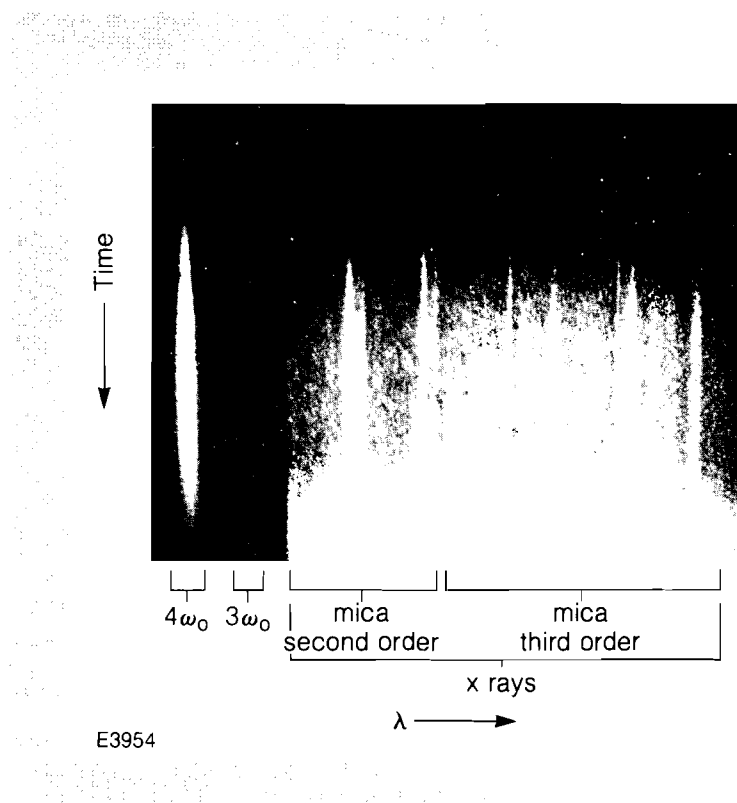
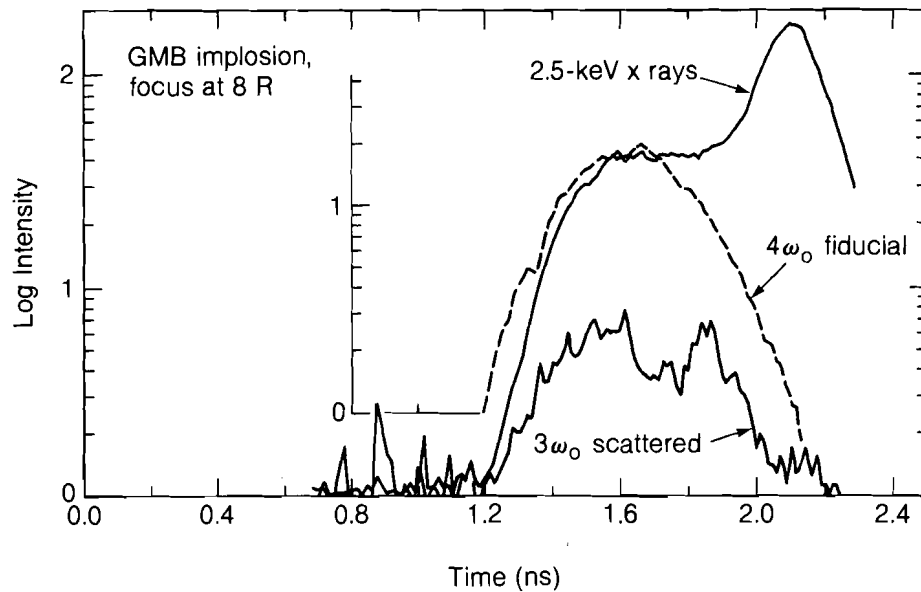


Fig. 28.5
Streak record showing the optical fiducial and x-ray spectrum from a glass microballoon target shot. The prominent x-ray spectral features are the silicon resonance lines: He_α and H_α in second order, and He_β , H_β , H_γ in third order off a mica analyzer crystal.



E3952

*Fig. 28.6
Overlay of the x-ray and optical fiducial signals, as reduced from Fig. 28.5.*

at 2.1 ns is the contribution from the x-ray continuum that is emitted during and after the implosion. Here, we define the implosion as the time corresponding to the minimum shell radius. The $4\omega_0$ signal (dashed line in Fig. 28.6) is more representative of the actual incident laser pulse shape. The lineout on the figure is positioned according to our best estimate (± 20 ps) of the timing of the laser pulse with the x-ray and $3\omega_0$ signals, which are synchronized.

Through these optical fiducials we can now synchronize the streak records from various x-ray streak cameras to each other and to the incident laser pulse.

ACKNOWLEDGMENT

This work was supported by the U.S. Department of Energy Office of Inertial Fusion under agreement No. DEFC08-85DP40200 and by the Laser Fusion Feasibility Project at the Laboratory for Laser Energetics, which has the following sponsors: Empire State Electric Energy Research Corporation, General Electric Company, New York State Energy Research and Development Authority, Ontario Hydro, Southern California Edison Company, and the University of Rochester. Such support does not imply endorsement of the content by any of the above parties.

REFERENCES

1. T. J. Goldsack *et al.*, *Phys. Fluids* **25**, 1634 (1982).
2. J. A. Tarvin *et al.*, *Phys. Rev. Lett.* **51**, 1355 (1983).
3. M. C. Richardson, R. S. Marjoribanks, S. A. Letzring, J. M. Forsyth, and D. M. Villeneuve, *IEEE J. Quantum Electron.* **QE-19**, 1861 (1983).

4. J. D. Kilkenny, O. Landen, S. D. Tabatabaei, J. Wark, O. Willi, A. Hauer, and C. J. Hooker, Rutherford Appleton Laboratory Annual Report RAL-84-049, 1984, p. A1-19 (unpublished).
5. R. S. Marjoribanks, M. C. Richardson, J. Delettrez, S. Letzring, W. Seka, and D. M. Villeneuve, *Opt. Commun.*, **44**, 113 (1982).
6. B. L. Henke and P. A. Jaanimagi, *Rev. Sci. Instrum.*, **56**, 1537 (1985).
7. P. A. Jaanimagi, B. L. Henke, and M. C. Richardson, *High Speed Photography, Videography, and Photonics III* (SPIE, Bellingham, WA, 1985), Vol. 569, p. 159.
8. B. L. Henke, J. P. Knauer, and K. Premaratne, *J. Appl. Phys.*, **52**, 1509 (1981).
9. R. Garron, *Ann. Phys. (Paris)*, **10**, 595 (1965).
10. C. P. Hale, H. Medecki, and P. H. Y. Lee, Lawrence Livermore National Laboratory Report UCRL-90089 (1984).

2.B Thermodynamics of a Polarizable One-Component Plasma

Introduction

The thermodynamic properties of dense plasmas, of electron density 10^{22} to 10^{26} cm^{-3} , in the temperature range 1 eV to 1 KeV, are not well known. At these high densities, the ion-ion interactions are very strong and generally their contribution to the plasma free energy cannot be regarded as minor.

Further, the ion interactions cannot be easily treated in terms of conventional two-body collision integrals because a typical ion is actually in "strong" collision with several neighboring ions simultaneously. A strong collision is one in which an appreciable part of an ion's kinetic energy is converted into potential energy during the collision. A measure of the importance of strong collisions is provided by the parameter $\Gamma = Ze^2/akT$ (where a is the ion sphere radius, given by $4\pi n_i a^3/3 = 1$). When $\Gamma > 1$, in effect, an ion is always in the strong collision regime; for our purposes the region of interest is $10 > \Gamma > 0.1$.

In addition, the electron-ion interactions contribute appreciable binding energy. Electrons tend to bunch around ions, providing shielding for the ions. This shielding is not very important at extremely high densities because the electrons are then quite degenerate and the Fermi energy (measured by the parameter $b = \mu/kT$, where μ is the chemical potential) greatly exceeds the interaction energy (measured by Γ), resulting in electrons that are fairly uniformly distributed throughout the plasma. At lower densities (measured by the parameter $b/\Gamma \sim 1$), and

at higher temperatures or smaller values of Γ , electrons are only partially degenerate and bunching around ions takes place, thereby polarizing the plasma.

High-density plasmas have been represented by a model consisting of pointlike ions embedded in a uniform electron background, called the one-component plasma (OCP). The OCP has been studied intensively by a number of investigators¹ because it simulates low temperature, high density, and fully ionized plasmas — yet its thermodynamic properties are simplified, being a function of just the one parameter Γ . Monte Carlo techniques are used to evaluate the complicated ion-ion interactions. While the OCP can model very high-density plasmas, its range of applicability can only be determined by comparison with a more physical plasma model. In our present work we do so and find that deviations in the estimates of the internal energy and pressure start appearing when the ion density falls appreciably below $9 \times 10^{28} \text{ cm}^{-3}$. The purpose of these calculations is to supplement these classical OCP investigations by determining the thermodynamic properties of dense plasmas that are only partially degenerate. This work extends similar calculations by DeWitt and Hubbard² and Totsuji and Takami.³ An additional purpose is to determine radial distribution functions for partially degenerate plasmas; these can be used for testing theoretical methods of calculating plasma properties.

The Calculation

The thermodynamic properties result from evaluation of derivatives of the free energy, or of the partition function, with respect to temperature and density. To evaluate $U = -(\partial \ln \hat{Z} / \partial \beta)_V$, $\beta P = (\partial \ln \hat{Z} / \partial V)_T$, etc., we start with N pointlike ions and the expression for the partition function:

$$\hat{Z} = e^{-\beta F_{\text{ions}}} \cdot \int \frac{d^{3N}R}{V^N} e^{-\beta U_{ii}} \text{Tr} [e^{-\beta(K_e + U_{ee} + U_{ie})}] . \quad (1)$$

The plasmas are assumed completely ionized; this assumption limits the applicability of the present phase of this work. Following a procedure discussed by Ashcroft and Stroud,⁵ the trace in the integral may be evaluated when the electron density fluctuations are linear in the electric potential, as, for instance, $\delta \tilde{\rho}(k) = q^2 \eta(k) \tilde{\varphi}(k)$ (where the tilde signifies the Fourier transform), and the Helmholtz free energy can then be calculated.

The dielectric function was calculated using the linear form of a density matrix, a procedure developed by March and Murray;⁶ this gives

$$q^2 \eta(k) = \frac{4}{\pi a_{\text{Bohr}} k} \int_0^\infty \frac{k'}{1 + \exp[\beta[E(k') - \mu]]} \ln \left| \frac{k + 2k'}{k - 2k'} \right| dk' . \quad (2)$$

Here, μ is the chemical potential and $k^2[\epsilon(k) - 1] = q^2 \eta(k)$.

This form is in agreement with the random phase approximation (RPA) dielectric function used by Totsuji and Takami.³ The potential closely approximates $\exp(-qr)/r$, where q is the Thomas-Fermi wave number. There are additional oscillatory terms, of order r^{-3} , which amount to a few percent for values of r that are of interest (see Fig. 28.7). These minor Friedel oscillation terms can provide long-term coupling of the plasma at distances greater than a few ion-sphere radii.

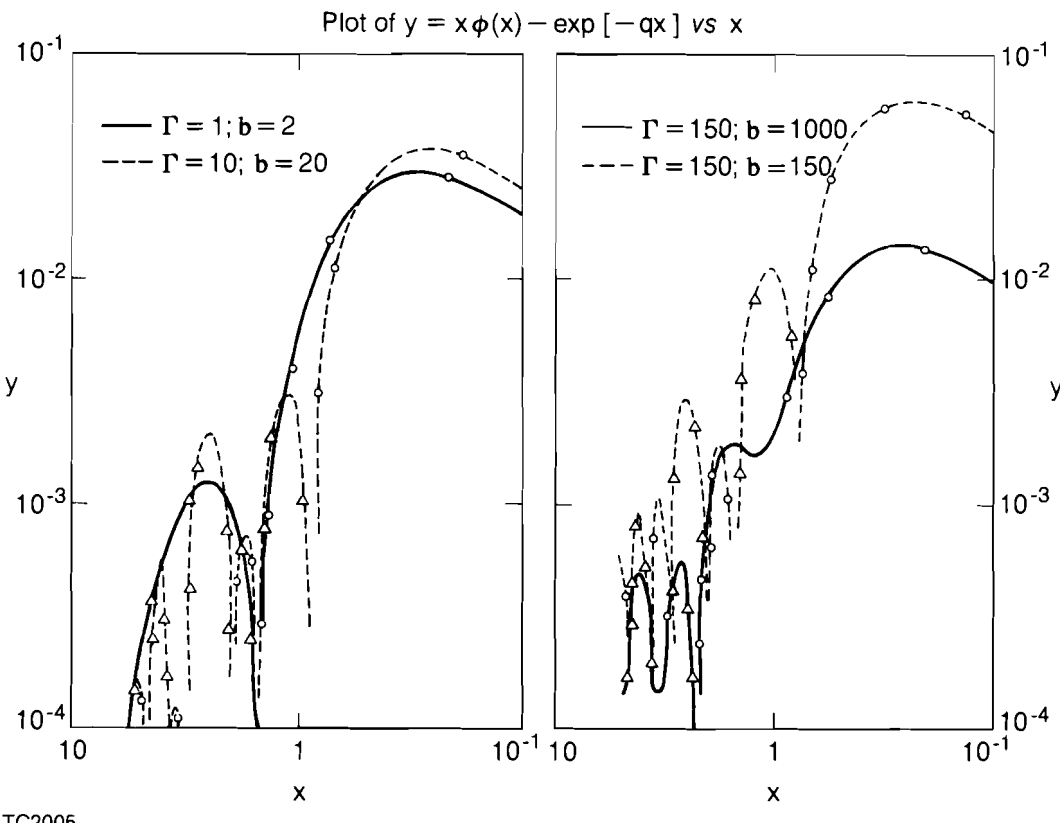


Fig. 28.7

Departures of the calculated potential from a Yukawa potential. Here, $x = r/a$, where a is the ion-sphere radius. (The usual plasma density parameter, $r_s = a/a_{Bohr}$, is given by $r_s \sim 2 \Gamma/b$.)

One gets \hat{Z} in a form useful for performing a Monte Carlo calculation:

$$\hat{Z} = e^{-\beta[F_{(\text{ideal ions})} + F_{(\text{free electrons})} + F_{\text{pol}}]} \cdot \int \frac{d^{3N}R}{V^N} e^{-\beta U_{\text{eff}}}, \quad (3)$$

where $\beta U_{\text{eff}} = \frac{1}{2} \beta \left\{ \sum_{I \neq J} Z_I Z_J \phi(|R_I - R_J|) \right.$

$$\left. + \sum_I Z_I^2 \lim_{\xi \rightarrow 0} [\phi(\xi) - \frac{1}{\xi}] \right\}, \quad (4)$$

and

$$\tilde{\phi}(k) = \frac{4\pi}{k^2 + q^2 \eta(k)} \quad (5)$$

For the plasmas presently being considered, F_{pol} is a small second-order term that can be ignored. The calculations use an Ewald sum technique for calculating U_{eff} and evaluating the pair distribution function. In effect, the plasma is represented as a cubic lattice, with N ($= 128$) ions per cell. For details, see Ref. 7.

In addition to the ordinary internal energy and pressure terms associated with noninteracting electron and ion gases, there are excess energy and pressure terms attributable to the interactions; these are

$$\frac{\beta U_{excess}}{N} \approx \left\langle \frac{\beta U_{eff}}{N} \right\rangle ; \quad (6)$$

$$\frac{\beta VP_{excess}}{N} \approx \frac{1}{3} \left(1 + \frac{1}{2} \langle qr \rangle \right) \left\langle \frac{\beta U_{eff}}{N} \right\rangle + \frac{1}{12} Z^2 \Gamma q^* a ; \quad (7)$$

where $\langle U_{eff}/N \rangle$ and $\langle qr \rangle$ are quantities resulting from the Monte Carlo calculation, and q^* is calculated from the limiting value of the effective two-body potential when $r \rightarrow 0$. Here, a is the ion sphere radius.

Results

Figure 28.8 shows the excess-energy term. It has been divided into two parts: (1) the energy per ion of a reference rigid body-centered cubic lattice (BCC); and (2) the difference in energy per ion between the plasma and the BCC lattice.

At large Γ the BCC lattice energy dominates. The BCC excess energy decreases from the OCP value as the density decreases. This reflects the binding energy of the electrons as they cluster around individual ions. For the plasmas studied, the difference in excess energy, plasma to lattice, also decreases with density, amounting to 0.5 kT per ion at ion densities of $2 \times 10^{23} \text{ cm}^{-3}$ (for $Z = 1$). The difference in energies is not a strong function of Γ at low densities. The very low-density, high- Γ models may be quite unphysical because deionization is not taken into account; for these models the plasma excess energy is less than that of the BCC lattice.

The excess-pressure terms must be tabulated. For the OCP, the terms involving q and q^* are absent in the expression for the excess pressure. The extra terms can cause the excess pressure to be more negative by up to 20% than in the OCP case. The calculations show that the following crude approximations may be used:

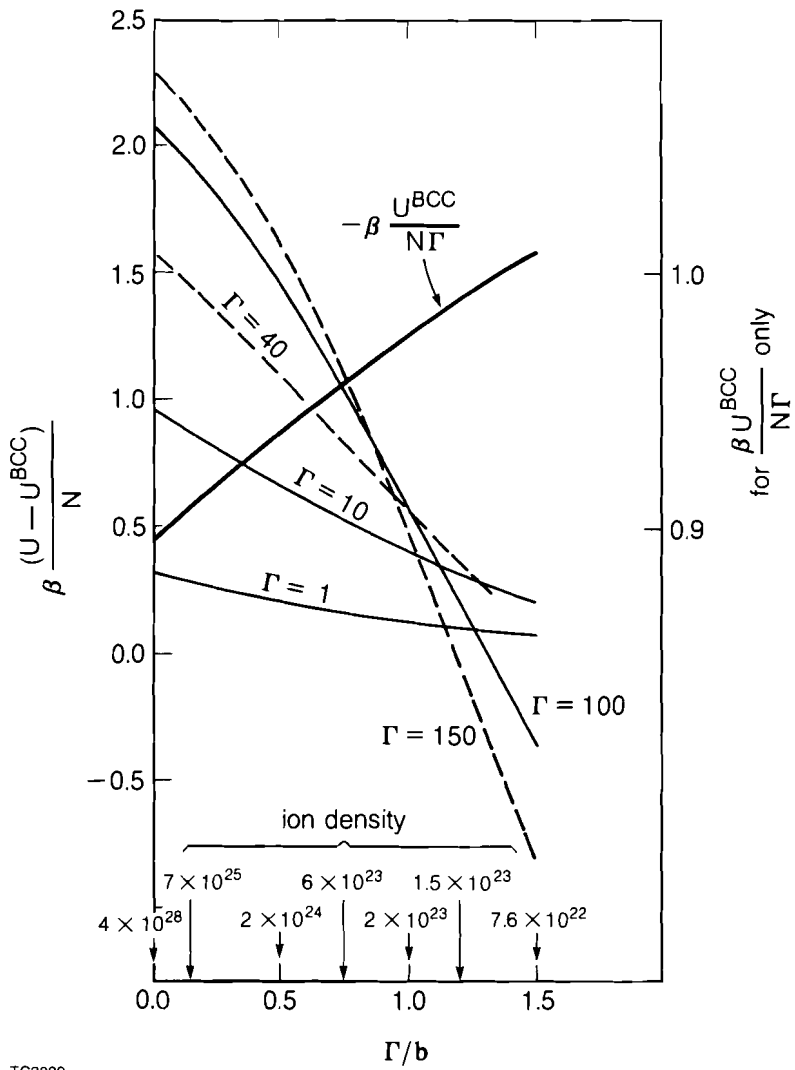


Fig. 28.8
Excess energies vs $\Gamma/b (= \Gamma kT/\mu \approx 0.5r_s)$.
The heavy solid line refers to a reference
BCC lattice and the scale on the right. The
other curves, for constant Γ , refer to the
scale on the left.

and

$$\langle \frac{\beta U_{\text{eff}}}{N} \rangle \sim - (0.9 + 0.033r_s) \Gamma Z^2 \quad \text{where } r_s = a/a_{\text{Bohr}}, \quad (8)$$

The pair-correlation functions show some unusual features (see Fig. 28.9). The minor oscillations beyond the first maximum first decrease in amplitude as one goes to lower densities and then increase in strength

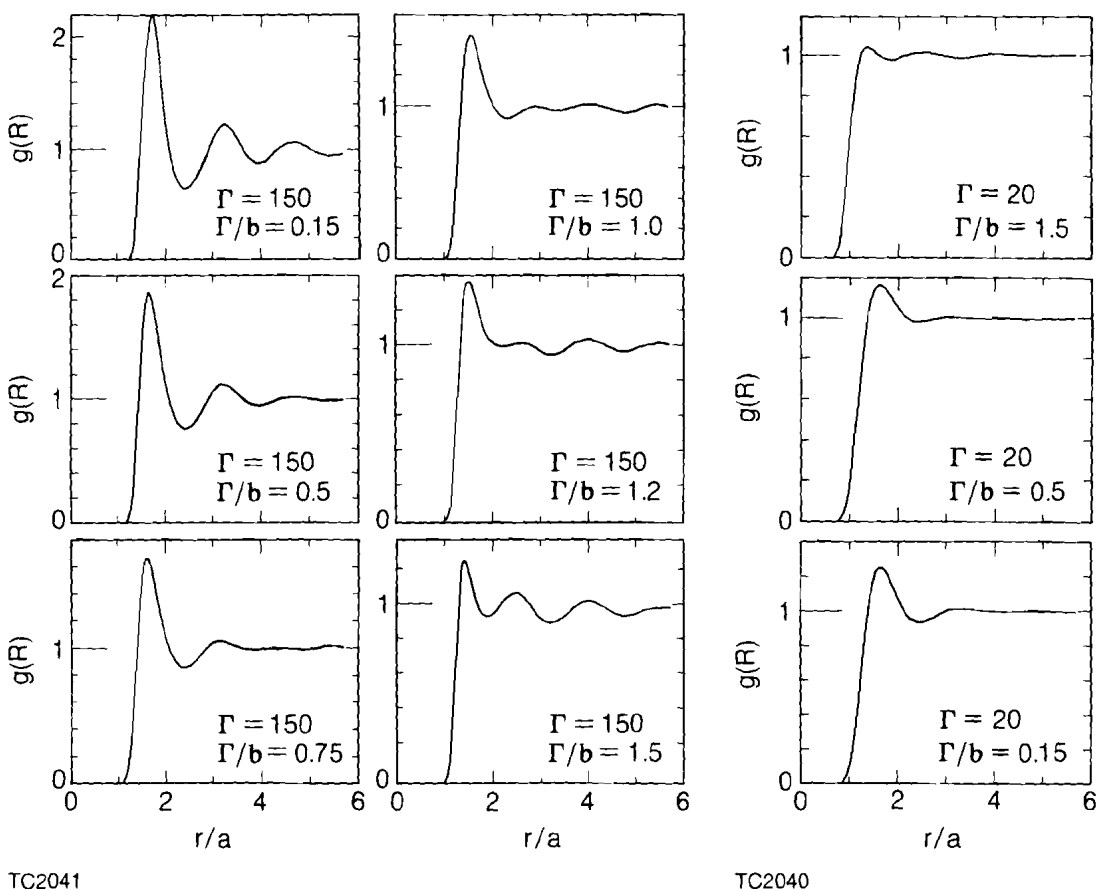


Fig. 28.9

Pair-correlation functions vs r/a , where a is the ion-sphere radius. The various curves are labeled by a density parameter (see Fig. 28.8).

(with a phase shift) as one goes to the lowest densities studied. This behavior is for all the models, down to the lowest value of Γ for which the oscillations can be studied. A modern theoretical interpretation, based on using the modified hyper-netted chain equation, will be tried in the future.

This work is basically complete from $\Gamma = 200$ to 1, and $r_s = 0$ to 3 (here $r_s = a/b_{\text{Bohr}}$) and for $Z = 1$. The extension to the extremely interesting high-temperature regime, $\Gamma = 0.01$ to $\Gamma = 1$, requires supercomputer time because extensive tables must be stored in order to calculate the necessary temperature and density derivatives.

ACKNOWLEDGMENT

The work was supported by the National Science Foundation under grant No. PHY-8406878.

REFERENCES

1. J. P. Hansen, *Phys. Rev. A* **8**, 3096 (1973); W. L. Slattery, G. D. Doolen, and H. E. DeWitt, *ibid.* **21**, 2089 (1980); **26**, 2255 (1982).
2. H. E. DeWitt and W. B. Hubbard, *Astrophys. J.* **168**, 131 (1976).
3. H. Totsuji and K. Tokami, *Phys. Rev. A* **30**, 3175 (1984).
4. F. J. Rogers, D. A. Young, H. E. DeWitt, and M. Ross, *Phys. Rev. A* **28**, 2990 (1983).
5. N. W. Ashcroft and D. Stroud, *Solid State Phys.* **33**, 2 (1978).
6. N. March and A. Murray, *Phys. Rev. A* **120**, 830 (1961); *Proc. R. Soc. London, Ser. A* **261**, 119 (1961).
7. H. L. Helfer, R. L. McCrory, and H. M. Van Horn, *J. Stat. Phys.* **37**, 577 (1984).

2.C Laser-Fusion-Target Implosion Studies with OMEGA

A major program to demonstrate the feasibility of direct-drive laser fusion is presently under way at LLE. A goal of this program is to compress deuterium-tritium (DT) fuel to 200 times its liquid density (200 XLD) by ablatively driving a target with the 24 UV (351-nm) beams of the 2-kJ OMEGA laser system. To reach these high fuel densities, targets consisting of cryogenically cooled fuel contained within thin shells of plastic or glass will be used.

Preliminary to the use of cryogenically cooled targets, numerical simulations have been performed^{1,2} to identify target designs that would enable generation of high neutron yields and modest fuel densities (~ 50 XLD). Initial experiments on these types of targets have resulted in neutron yields of as much as 2×10^{11} (spring 1985) for high-yield targets and final densities of ~ 30 XLD for high-density targets.^{3,4} These experiments provided the necessary conditions to test instrumentation that will be required to diagnose the performance of targets used in the 200-XLD campaign and to examine the performance of the targets relative to one-dimensional hydrodynamic code simulations.

In this report we summarize further direct-drive (high-yield) target implosion studies performed with the 24 UV (351-nm) beams of the 2-kJ OMEGA laser system (spring 1986). Targets consisted of glass microballoons (GMB) having initial aspect ratios ($R/\Delta R$) of $\sim 200\text{--}300$ and equimolar fills of deuterium and tritium at a pressure of 10 atm. Neutron yields as high as $\sim 3 \times 10^{11}$ were produced by accelerating these low-mass shells to high velocities, thereby producing core temperatures of ~ 5 keV and fuel densities of ~ 1 XLD. Diagnosis of

target performance during the acceleration phase of the target implosions was obtained from time- and space-resolved measurements of the x-ray emission from the laser-heated glass shells. Target performance during the deceleration or stagnation phase of the implosions was diagnosed by nuclear and particle instrumentation, from which estimates of total thermonuclear yield, fuel temperature, and fuel and shell densities were obtained.

The x-ray emission from the laser-heated glass microballoons was imaged by x-ray microscopes⁵ and an imaging x-ray streak camera with an optical fiducial.⁶ Plotted in Fig. 28.10 is the radius of the maximum x-ray emission versus time, determined from a streak camera image of a target implosion. Also plotted is the one-dimensional hydrodynamic-code (*LILAC*) predicted radius versus time, along with the idealized laser pulse, whose position was determined by reference to the optical fiducial. The measured radius of the target versus time, thus determined, follows the *LILAC* prediction fairly closely. However, the spatial distribution of the x-ray emission from time-integrated, x-ray microscope images shows departures from predictions; these departures correlate with initial target wall thickness. Figure 28.11 shows azimuthally averaged radial profiles determined from the x-ray images of a series of target implosions (including the example of Fig. 28.10). The targets in this series had almost the same initial radii but different wall thicknesses. The thinner-walled targets [Figs. 28.11(c) and 28.11(d)] produced time-integrated, radial x-ray profiles that deviated from the *LILAC*-predicted profiles by a larger extent than did the thicker-walled targets [(Figs. 28.11(a) and 28.11(b))]. Simulations using *LILAC* show that such modified profiles occur if the intensity on the target is higher than that of the measured average value.

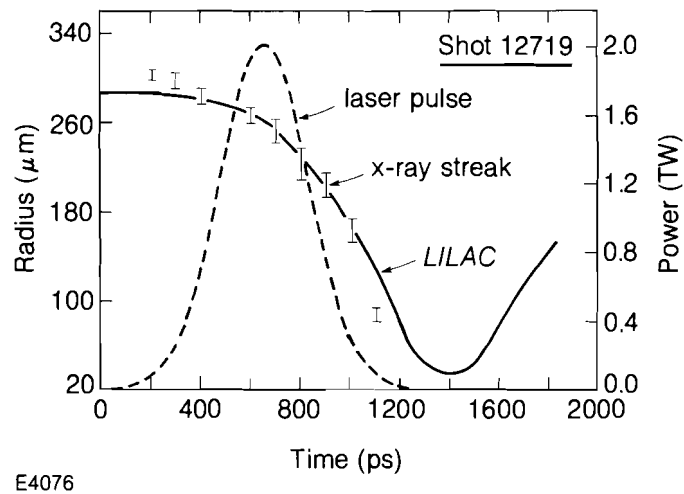
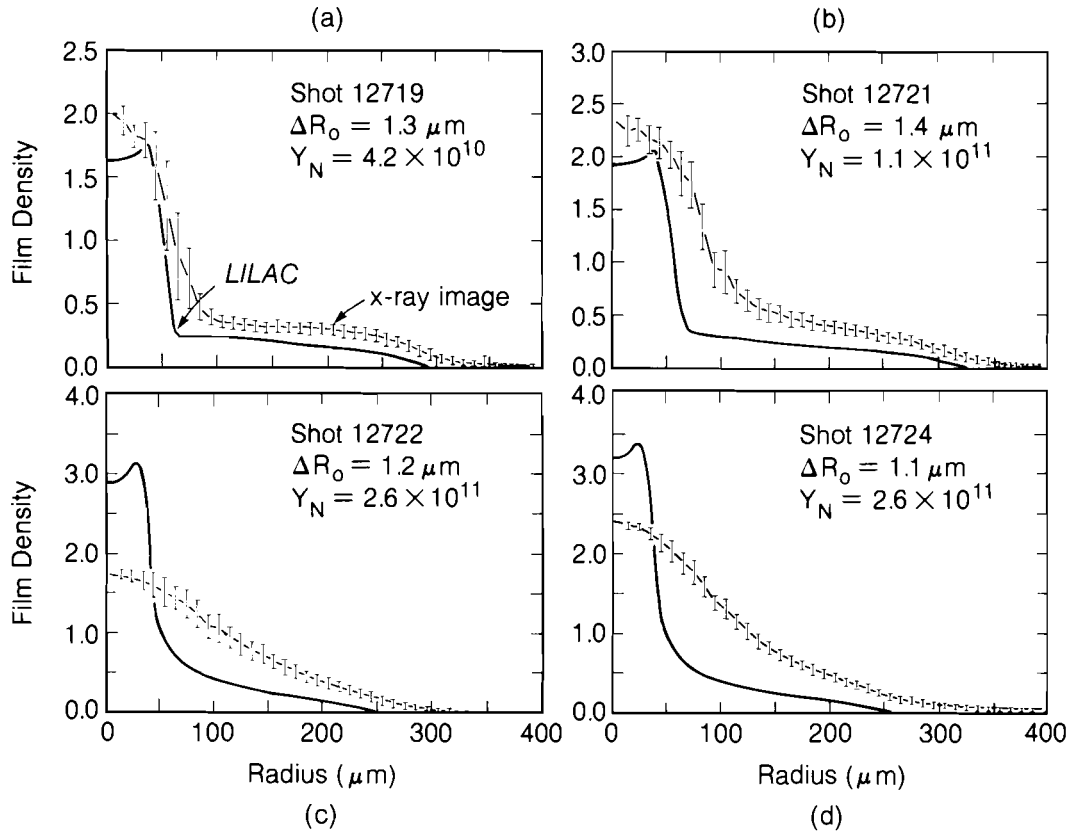


Fig. 28.10

The radius of the target versus time, as determined from the separation of the x-ray emission coming from opposite sides of the target, viewed by an x-ray streak camera with an imaging pinhole. *LILAC* simulations of the same are also shown.



E3972

Fig. 28.11

Averaged radial profiles determined from time-integrated x-ray micrographs of target implosion. The LILAC simulations take into account the response of the microscopes and film. (a) and (b) are examples of thicker shells; (c) and (d) are examples of thinner shells.

Further indirect evidence of departures from predicted one-dimensional behavior that are more pronounced for thin-walled targets is seen in time-resolved, soft x-ray emission measurements made with a four-channel, 3-GHz, x-ray-diode spectrometer (MINIFLEX).⁷ Figure 28.12 shows the time-resolved x-ray emission (around $E \sim 1 \text{ keV}$) for the implosions of Fig. 28.11, as resolved by one of the fast x-ray photodiodes. LILAC simulations of the MINIFLEX response are also shown. The x-ray signal versus time is close to that predicted for the thicker-walled targets [Figs. 28.12(a) and 28.12(b)], the main features of which are emission coming from the glass shell during the laser pulse, and subsequent reheating of the shell, which occurs during the final stage of the implosion. The width of the stagnation peaks is significantly broader than the instrumental response time ($\sim 100 \text{ ps}$). The thinner-walled targets [Figs. 28.12(c) and 28.12(d)] show very little emission at the predicted time of stagnation, indicating that the shells had been

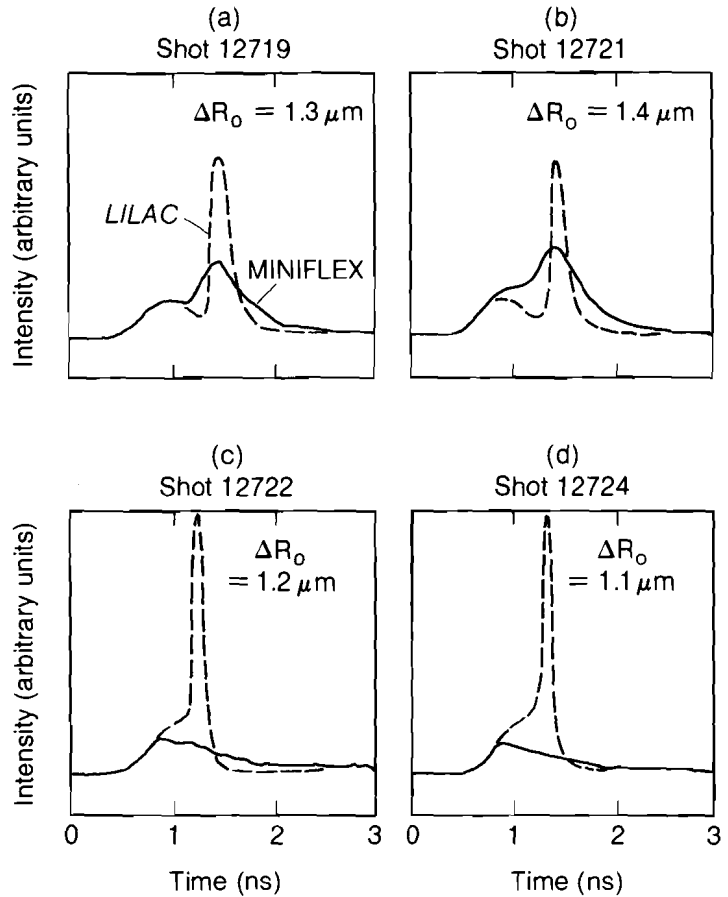


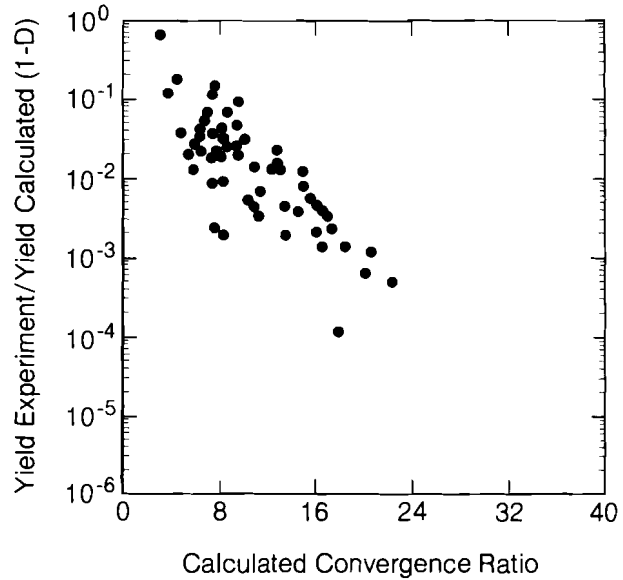
Fig. 28.12
Time-resolved, spatially integrated x-ray emission from the targets whose radial profiles are shown in Fig. 28.11, as resolved by the MINIFLEX system.

ablated away, had broken up, or had stagnated over a longer time. LILAC simulations of these implosions indicate that sufficient shell material in a thin shell should remain, so that a pronounced x-ray stagnation peak is predicted in all cases. In contrast, the shell radius versus time during the implosion appears to be correctly predicted by LILAC for the thinner-walled targets as well as for the thicker-walled targets, indicating that the predicted mass-ablation rate is close to the actual average mass-ablation rate. This points to something other than the average intensity (such as nonuniformities in the target illumination) as the cause for the apparent burn-through or breakup of shell material in the case of the thinner-walled targets.

The overall performance of the targets during the stagnation phase of the implosion is characterized by the neutron yield. Figure 28.13 shows the ratio of the measured and LILAC-predicted neutron yields versus the calculated convergence ratio. (The convergence ratio is defined as the ratio of the initial fuel radius divided by fuel radius of the stagnated core.) The result closest to the LILAC-predicted yield (~70%) was

Fig. 28.13

Normalized neutron yield (ratio of experimentally measured neutron yield to calculated neutron yield) versus the calculated target convergence ratio (convergence ratio is defined as the ratio of the initial to the final target radius).



E4077

obtained for a target that had a calculated convergence ratio of only 3.2. As previously noted,² the declining agreement between measured and predicted neutron yields at higher predicted convergence ratios is an indication of the presence of implosion nonuniformities (which are estimated to be $\sigma_{rms} \sim 20\%$ for these experiments).

Time-integrated images of the alpha-particle emission were obtained by the technique of zone-plate imaging.^{8,9} Figure 28.14(a) shows a composite of an x-ray image and alpha-particle image obtained on a single shot. Figure 28.14(b) shows equivalent one-dimensional profiles of these images, together with LILAC-predicted profiles. The extent of the alpha emission region is seen to lie within the LILAC-predicted x-ray emission profile, the latter being a good indicator of the predicted position of the shell material at stagnation. The alpha image profile (radially averaged) also matches the LILAC-predicted profile, although nonspherical features are seen in the image. The absolute magnitude of alpha-particle flux was normalized to the measured total neutron yield, which is smaller than the predicted value by a factor of 8.5. In general, the alpha emission region, where thermonuclear burning takes place, has a size comparable to that predicted. The alpha images indicate, however, that the burning region is not always spherically symmetric and sometimes there are several peaks in the alpha emission indicative of asymmetries in the imploded core. These asymmetries occur more often in the case of targets with thicker walls.

The fuel ion temperature (T_i) obtained during the time of thermonuclear burning was estimated by the technique of neutron time-

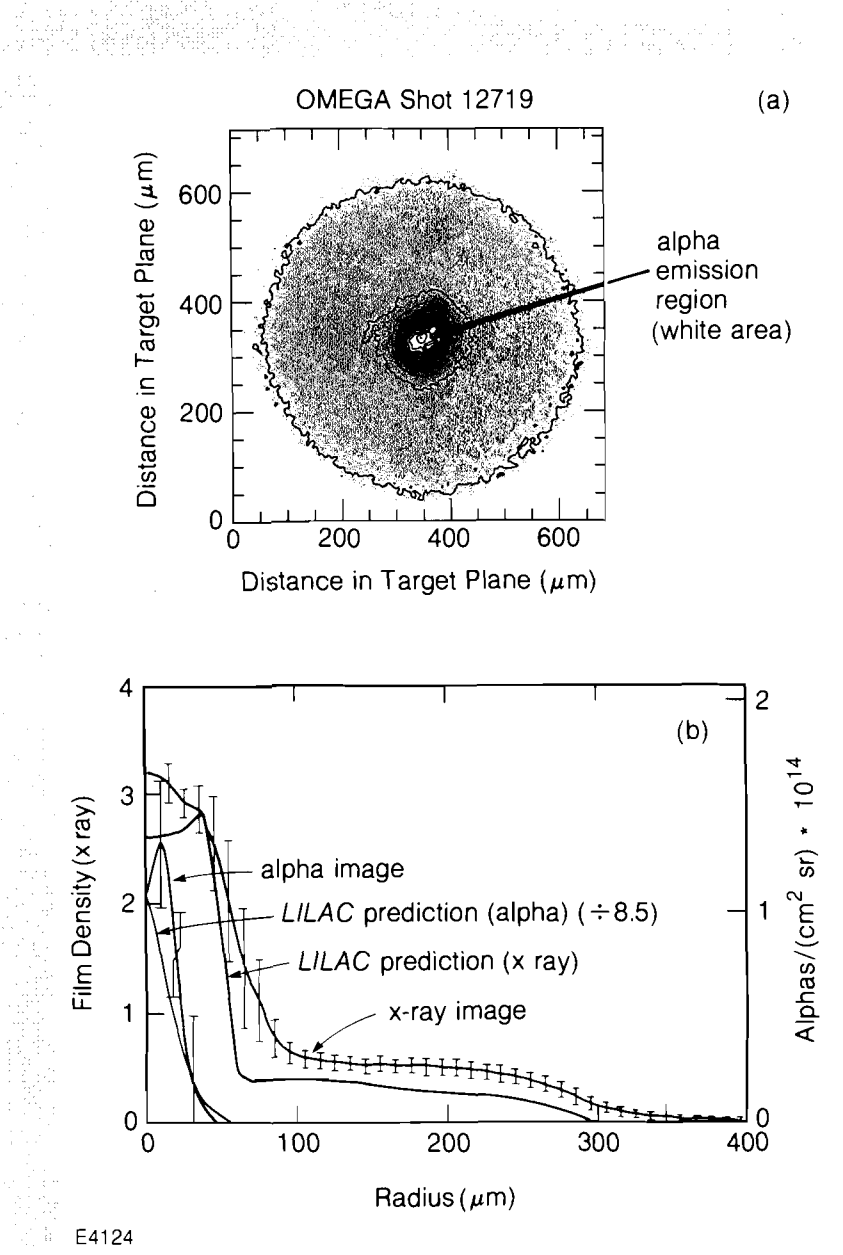


Fig. 28.14
 (a) Composite of an x-ray micrograph (around $E=4$ keV) of a high-yield target implosion and an alpha zone-plate image indicating the spatial distribution of the alpha particle products of thermonuclear burning.
 (b) Averaged radial profiles of the images in (a), together with LILAC postprocessor predictions of the same.

of-flight (NTOF).¹⁰ The NTOF-measured T_i for the target shots of Fig. 28.11 fall into two extremes. The thicker-walled targets [Figs. 28.11(a) and 28.11(b)] have NTOF-inferred T_i of 4.0 and 4.2 keV, respectively, as compared to LILAC predictions of 3.8 and 4.2 keV. The thinner-walled targets [Figs. 28.11(c) and 28.11(d)] have NTOF-inferred T_i of 10.9 and 14.4, while the LILAC predictions are 6.1 and 7.3 keV. The NTOF-inferred T_i are far in excess of the predicted temperatures for the thin-walled targets.

Two-dimensional hydrodynamic simulations of nonuniformly illuminated targets indicate⁴ that at stagnation shell material may be

transported into the fuel, lowering T_i and decreasing the thermonuclear yield. Although inferred T_i for thin-walled targets appears higher than predicted (rather than lower), the increase in the width of the NTOF signal may be due to Doppler broadening by differential bulk motion of the fuel material, or by differences in ion temperature due to the existence of several separate burning regions. As an example, the 14.4-keV temperature inferred for shot 12724 could be explained by fuel in a burning shell that is moving radially inward at a velocity of $\sim 6 \times 10^7$ cm/s, a velocity comparable to the maximum velocity of the shell.

To summarize the measurements of target implosion behavior: (1) The average shell velocity appears to be well modeled in the acceleration phase of the implosion. However, velocity errors introduced by small-scale illumination nonuniformities may explain deviations from this average. (2) Measured, stagnated-shell sizes appear to agree more closely with *LILAC* calculations for those targets having thicker walls, although deviations from spherically symmetric implosions are evident. (3) Inferred T_i deviate from calculated T_i for those targets whose x-ray measurements are indicative of in-flight shell burn-through or breakup.

The NTOF-measured T_i , the $\langle \rho_f \rangle$ inferred from alpha images, and the measured neutron yield Y_N can be compared for consistency by assuming that Y_N is given by

$$Y_N = \frac{n_{DT}^2}{4} \langle \sigma v \rangle \tau_d V , \quad (1)$$

where n_{DT} is the number density of DT pairs, $\langle \sigma v \rangle$ is the velocity cross-section product averaged over the distribution of velocities, τ_d is the disassembly time, and V is the volume of the burn region. An estimate of the disassembly time is

$$\tau_d = R_f / C_s , \quad (2)$$

where R_f is the radius and C_s is the sound speed, both pertaining to the burn region. The sound speed is given by

$$C_s = (\gamma_e P_e + \gamma_i P_i)^{1/2} \rho^{-1/2} , \quad (3)$$

where γ is the ratio of specific heats, P_e and P_i are the electron and ion partial pressures, and ρ is the density.

Assuming $\gamma_e = \gamma_i = 5/3$ and $T_i \sim T_e$, the sound speed is given by

$$C_s = 3.6 \times 10^7 T_{\text{keV}}^{1/2} \text{ cm s}^{-1} . \quad (4)$$

The DT-pair number density can be estimated by assuming that a fraction f of the fuel is confined to a region whose size is equal to the size of the alpha image, R_α :

$$n_{\text{DT}} = \rho f (R_i/R_\alpha)^3 / (m_D + m_T) . \quad (5)$$

Taking the measured quantities of T_i , R_α , and Y_N and assuming $f \sim 1$ we can solve for the implied confinement time τ_d . Values of τ_d thus obtained are found to be of the order of a few picoseconds for the shots in Table 28.I. The values of the confinement time τ_d^* , calculated by assuming that the fuel is confined to a region of size R_α for one sound-speed crossing time, are listed in column 10 of Table 28.I. The yield-implied confinement times are seen to be unphysically small as compared to hydrodynamic time scales (i.e., the sound-speed crossing time). Alternatively, if we take the measured quantities of T_i , R_α , and Y_N and assume that the confinement time is given by τ_d^* , we can solve for the implied fraction of fuel, which is contributing to the burn. These values are given in column 11 of Table 28.I. In all cases the fuel contributing to burning is implied to be a small fraction of the original fuel mass.

Table 28.I
High-yield-target measured and derived quantities.

(1) Shot No.	(2) $R_i(\mu\text{m})$	(3) $\Delta R_i(\mu\text{m})$	(4) $E_{\text{uv}}(\text{J})$	(5) Y_N (expt)	(6) Y_N (L/LAC)	(7) $T_i(\text{keV})$ (expt)	(8) $T_i(\text{keV})$ (L/LAC)	(9) $R_\alpha(\mu\text{m})$	(10) $\tau_d^*(\text{ps})$	(11) f
12714	240.8	1.20	1223	8.7×10^{10}	2.7×10^{12}	—	—	45	—	—
12719	285.8	1.34	1235	4.2×10^{10}	3.4×10^{11}	4.0	3.8	53	61	0.32
12721	307.6	1.39	1342	1.1×10^{11}	7.1×10^{11}	4.2	4.2	52	56	0.38
12722	246.6	1.20	1404	2.6×10^{11}	2.7×10^{12}	10.9	6.1	55	42	0.33
12724	255.4	1.09	1465	2.6×10^{11}	3.7×10^{12}	14.4	7.3	49	22	0.21

(1) shot number; (2) initial target radius; (3) initial target wall thickness; (4) incident laser energy; (5) measured neutron yield; (6) L/LAC -predicted neutron yield; (7) NTOF-inferred fuel ion temperature; (8) L/LAC -predicted fuel ion temperature; (9) measured alpha-particle emission region size; (10) sound-speed crossing time of fuel region; (11) fraction of fuel partaking in thermonuclear burning, assuming burn has duration of τ_d^* .

E4086

We see that the measured values of T_i , R_α , and Y_N cannot be used to consistently describe, in a simple way, the thermonuclear burn that takes place in these experiments. Rather, mixing of fuel and shell material due to illumination nonuniformities may be causing a reduction in confined fuel mass, systematically high inferred ion temperatures as well as reduced burn times. Improvement in target performance in future experiments should be evidenced by more consistent measured values of T_i , R_α , and Y_N .

ACKNOWLEDGMENT

This work was supported by the U.S. Department of Energy Office of Inertial Fusion under agreement No. DE-FC08-85DP40200 and by the Laser Fusion Feasibility Project at the Laboratory for Laser Energetics, which has the following sponsors: Empire State Electric Energy Research Corporation, General Electric Company, New York State Energy Research and Development Authority, Ontario Hydro, Southern California Edison Company, and the University of Rochester. Such support does not imply endorsement of the content by any of the above parties.

REFERENCES

1. P. W. McKenty and C. P. Verdon, LLE Theory Group Report No. 15 (1985).
2. LLE Review **25**, 7 (1985).
3. LLE Review **24**, 161 (1985).
4. M. C. Richardson, P. W. McKenty, R. L. Keck, F. J. Marshall, D. M. Roback, C. P. Verdon, R. L. McCrory, J. M. Soures, and S. M. Lane, *Phys. Rev. Lett.* **56**, 2048 (1986).
5. M. C. Richardson, R. S. Marjoribanks, S. A. Letzring, J. M. Forsyth, and D. M. Villeneuve, *IEEE J. Quantum Electron.*, **QE-19**, 1861 (1983).
6. G. G. Gregory, S. A. Letzring, M. C. Richardson, and C. D. Kiikka, in *High Speed Photography, Videography, and Photonics III*, edited by B. G. Porsegi and H. C. Johnson, (SPIE, Bellingham, WA, 1985), Vol. 569, p. 141.
7. LLE Review **25**, 20 (1986).
8. J. Wark (private communication).
9. N. M. Ceglio and L. W. Coleman, *Phys. Rev. Lett.* **39**, 20 (1977).
10. M. C. Richardson, P. W. McKenty, F. J. Marshall, C. P. Verdon, J. M. Soures, R. L. McCrory, O. Barnouin, R. S. Craxton, J. Delettrez, R. L. Hutchison, P. A. Jaanimagi, R. Keck, T. Kessler, H. Kim, S. A. Letzring, D. M. Roback, W. Seka, S. Skupsky, B. Yaakobi, and S. M. Lane, in *Laser Interaction and Related Plasma Phenomena Vol. 7*, edited by H. Hora and G. Miley (Plenum, New York, in press).

2.D Thermal Self-Focusing with Multiple Laser Beams

Self-focusing in the long-scale-length coronas of reactor targets may enhance undesired parametric processes and may lead to the degradation of drive uniformity. Both the ponderomotive and thermal modes are of potential importance. In this article our concern is primarily with the thermal mode, which is amenable to simulation using the hydrodynamics/ray-tracing code SAGE.^{1,2} Hydrodynamic simulations of thermal self-focusing have the advantage that the time history of the plasma under laser heating, thermal conduction, and two-dimensional hydrodynamic flow can be followed, in contrast to simple perturbation models in which (a) plasma properties vary in one dimension only (transverse to the laser propagation direction); (b) the perturbed temperature and density profiles are related by static pressure balance; and (c) refraction near critical is excluded.

For multibeam laser-irradiation systems such as OMEGA it is of interest to investigate self-focusing effects associated with multiple overlapping laser beams. While this is a fully three-dimensional problem, insight may be gained from two-dimensional simulations. Here we use Cartesian geometry, with variations of plasma parameters and ray trajectories permitted in the (x,y) plane. Cylindrical or spherical geometries could alternatively be used, with the laser beams treated as annular rings. The simulations presented here make use of a recent enhancement to SAGE whereby any number of independent laser beams may be specified, each with its own wavelength, temporal and spatial profiles, angle of incidence, and focusing parameters.

Thermal and Ponderomotive Self-Focusing

Models of self-focusing generally consider a uniform laser beam of wavelength λ and intensity I propagating through a plasma of electron temperature T_e , electron density n_e , and critical density n_c . It is assumed that superimposed upon the beam is an intensity perturbation, or "hot spot," with a wavelength λ_{\perp} transverse to the direction of propagation. In the simplest theory of ponderomotive self-focusing³ (sometimes known as filamentation), whether or not the perturbation will grow depends only on the balance between two physical processes, the ponderomotive force and diffraction. The ponderomotive force pushes plasma away from the higher-intensity portions of the beam, causing the beam in these regions to converge due to the resultant refractive-index change, and thereby enhancing the perturbation. Counteracting this tendency, diffraction always causes the higher-intensity portions to diverge. Whatever the parameters of the laser and the plasma, the theory predicts that there is a threshold wavelength λ_{th} such that no growth is possible for λ_{\perp} less than λ_{th} but growth occurs for any λ_{\perp} greater than λ_{th} . Maximum growth occurs for $\lambda_{\perp} = \lambda_p (= \sqrt{2} \lambda_{th})$:

$$\lambda_p = 3.273 \times 10^2 \left(\frac{T_e}{I} \frac{n_c}{n_e} \right)^{1/2} (1 - n_e/n_c)^{1/4} \text{ cm}, \quad (1)$$

where T_e is in eV and I in W/cm².

It is important to note that all plasmas are unstable to (ponderomotive) self-focusing, for sufficiently large perturbation wavelengths λ_{\perp} . The crucial parameter, however, is the growth length L through which the intensity perturbation is amplified by a factor of e . Significant growth may be expected if the scale length of the coronal plasma exceeds L . For maximum growth ($\lambda_{\perp} = \lambda_p$), the growth length is given by

$$L_p = 3.409 \times 10^4 \frac{T_e}{I\lambda} \left(\frac{n_c}{n_e} - 1 \right) \text{ cm}, \quad (2)$$

where λ is in centimeters. For larger transverse wavelengths ($\lambda_{\perp} > \lambda_p$), the growth length increases slowly ($L/L_p \approx 0.7 \lambda_{\perp}/\lambda_p$ for $\lambda_{\perp} \geq 2\lambda_p$).

A similar picture holds for thermal self-focusing, except that here it is the thermal pressure of heated plasma rather than the ponderomotive force that pushes the plasma laterally. In perturbation treatments⁴ the plasma temperature profile in the lateral direction is determined by balancing laser-energy deposition with thermal diffusion, and the density profile is then obtained assuming lateral pressure balance ($n_e T_e = \text{constant}$). While this treatment neglects time-dependent hydrodynamics, and uses Spitzer's formula⁵ for the lateral heat flux in a regime in which it almost certainly breaks down, it is nevertheless useful as a guide to the parameter regimes in which thermal self-focusing is liable to be found.

For thermal self-focusing there is a transverse wavelength threshold:

$$\lambda_T = 14.5 A_o^{1/2} \left(\frac{n_c}{n_e} \right)^{3/4} \frac{\lambda T_e^{5/4}}{Z^{1/2} I^{1/4}} \text{ cm}, \quad (3)$$

where Z is the ion charge state and A_o is a number close to unity. For perturbation wavelengths $\lambda_{\perp} < \lambda_T$ no growth occurs because diffraction is dominant. For $\lambda_{\perp} > \lambda_T$, the growth length is almost independent of λ_{\perp} and is given by

$$L_T = 67.0 A_o \left(\frac{n_c}{n_e} \right)^{3/2} \frac{\lambda T_e^{5/2}}{Z I^{1/2}} \text{ cm}. \quad (4)$$

As an illustration of the use of these formulae, Table 28.II gives the values of L_T , λ_T , L_p , and λ_p for a wavelength $\lambda = 250$ nm (krypton fluoride laser), $I = 10^{15}$ W/cm², and $Z = 3.5$ (CH), for two temperatures (6 keV and 1 keV) and two regions in the corona (quarter and tenth critical). The higher temperature would correspond to the peak of a shaped reactor pulse, and the lower temperature to the early, lower-intensity portion of the pulse. For $T_e = 6$ keV, the thermal growth

length L_T is very large, several times greater than the millimeter scale length anticipated for a reactor plasma. L_T may be an overestimate, however, because the assumption of Spitzer conductivity leads to an unreasonably strong temperature dependence [see Eq. (4)]. On the other hand, for $T_e = 1$ keV, L_T becomes much less than a millimeter. It therefore appears that thermal self-focusing is of greatest concern for target designs that result in the generation of a relatively cold long-scale-length plasma early in the pulse.

The ponderomotive mechanism is clearly important for both temperatures. Its effects may possibly be mitigated by using overlapping beams, so that a high average intensity on the surface of a sphere would be obtained from a large number of individual beams each with an intensity below the threshold for significant self-focusing. Alternatively, the use of ISI techniques⁶ may suppress self-focusing.

Table 28.II
Growth lengths and transverse wavelength (microns) for thermal and ponderomotive self-focusing.

	$T_e = 6$ keV				$T_e = 1$ keV			
	Thermal		Ponderomotive		Thermal		Ponderomotive	
	L_T	λ_T	L_P	λ_P	L_T	λ_T	L_P	λ_P
$n_c/4$:	3,380	51	240	15	40	5	40	6
$n_c/10$:	13,300	102	740	25	150	11	120	10

TC2078

Hydrodynamic Simulations

In a typical simulation [see Fig. 28.15(a)] a hot spot is represented by a 1.5-ns beam (full width at half maximum), with a nominal intensity of 3×10^{15} W/cm² based on the area in the target plane containing 90% of the energy. The beam is incident at an angle of 20° upon a cold preformed plasma with an exponential density profile of scale length 1 mm.

Here, as well as in subsequent simulations, the laser has a wavelength of 351 nm, and Gaussian temporal and spatial profiles. Rays are plotted up to the point at which 90% of their energy has been deposited, although their trajectories are calculated until all but one part in 10⁵ is absorbed. Only a subset of the rays actually used is plotted. The marginal rays have intensities that are 10% of the peak intensity; the beam is truncated beyond these bounds in order that the figures provide a useful representation of the spatial location of the beam energy. A flux limiter f equal to 0.04 is used.⁷ (The effect of varying the flux limiter was investigated in Ref. 1). By the peak of the pulse ($t = 0$), a self-focusing channel is apparent in the underdense plasma.

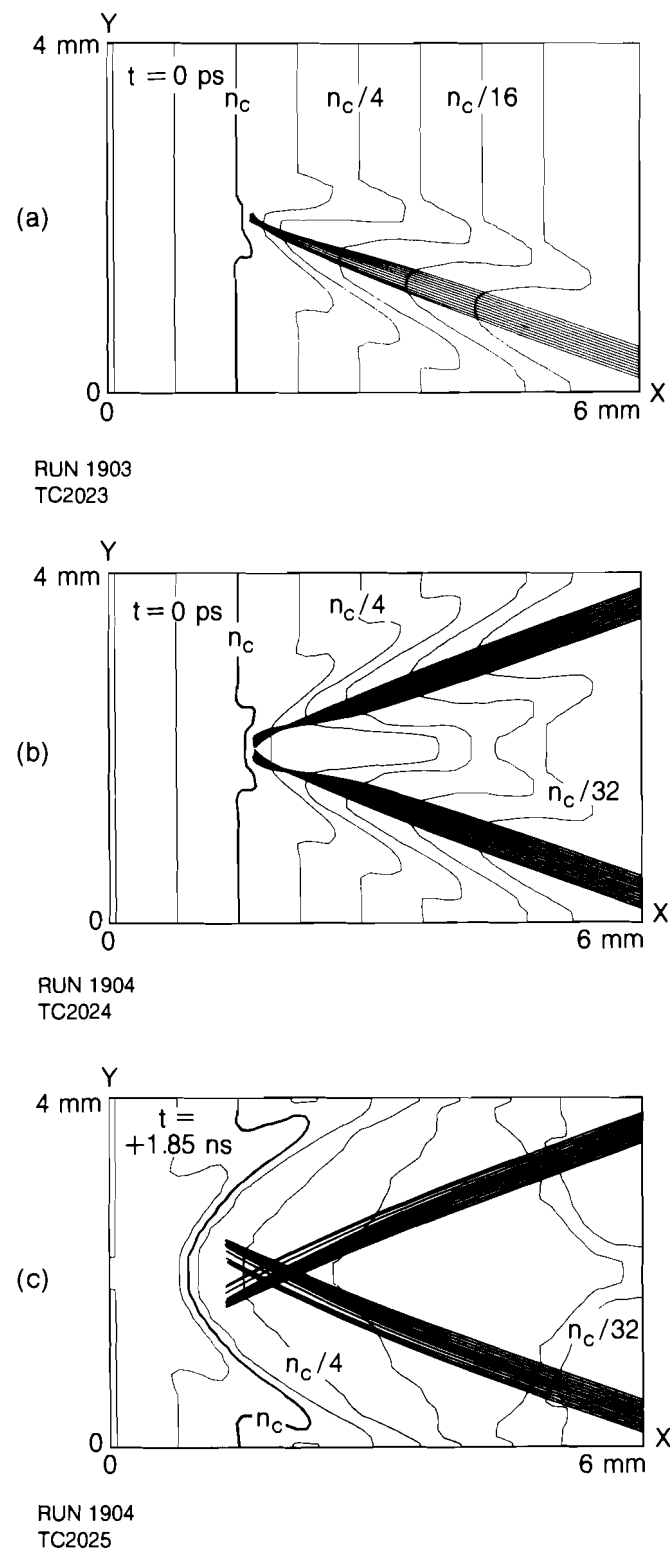


Fig. 28.15
Self-focusing of single and overlapping beams in a long-scale-length preformed plasma. In (a) a single beam is incident in Cartesian geometry at 20° to the target normal, forming a self-focusing channel in the corona. In (b) a second beam, identical except for the angle of incidence, is added. Two independent self-focusing channels are formed. At a later time (c), plasma ablation has removed the channels and the two beams propagate independently through the plasma.

In order to examine the effect of overlapping beams, a second beam, identical except for the angle of incidence, is added in Figs. 28.15(b) and 28.15(c). The two beams are pointed so as to overlap on the initial critical surface. At the peak of the pulse [$t = 0$, Fig. 28.15(b)], two largely independent channels are seen, with a high-density region formed between the two beams. Later in time [$t = +1.85$ ns, Fig. 28.15(c)], the channels have merged, plasma ablation has led to the termination of self-focusing, and the two beams pass through each other. The transient nature of thermal self-focusing is a characteristic feature of these and earlier simulations.¹

A second configuration of interest is that of a hot spot superimposed upon a beam of larger diameter. An example is provided in Fig. 28.16. In Fig. 28.16(a) a single beam of Gaussian spatial profile, diameter 1.2 mm and intensity 1.5×10^{15} W/cm², is seen not to self-focus, aside from a few marginal rays being refracted inward. This is as expected,

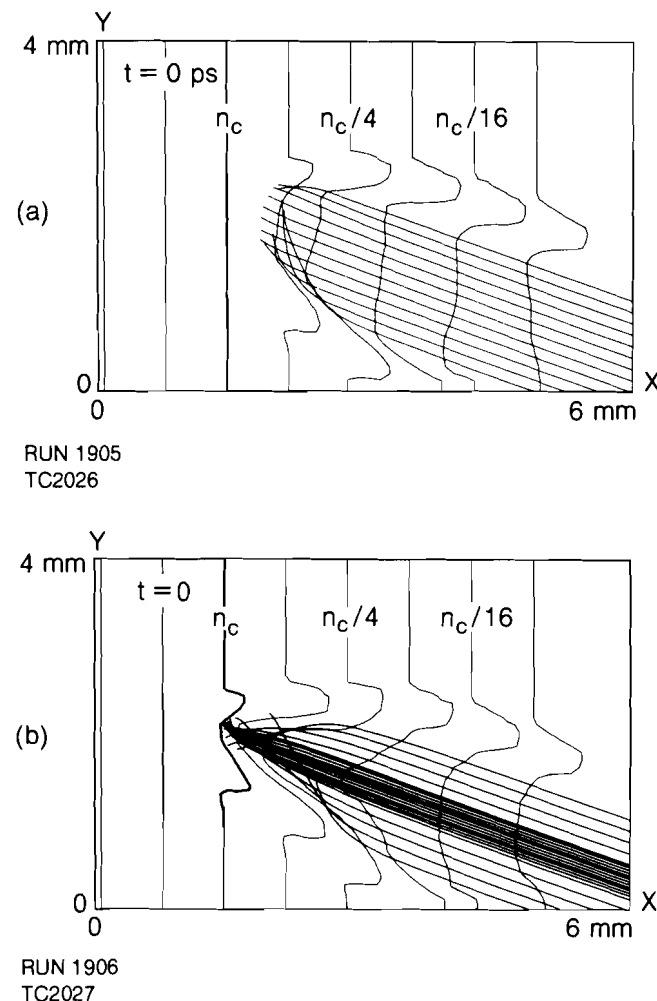


Fig. 28.16
Effect of a hot spot superimposed on a background beam. In (a) a broad background beam propagates through a long-scale-length preformed plasma largely unaffected by refraction. In (b), with 50% of the energy redistributed into a small-diameter hot spot, the hot-spot beam self-focuses and also causes rays from the background beam to be refracted in toward the focus.

because the beam diameter exceeds the plasma scale length.¹ For the simulation shown in Fig. 28.16(b), 50% of the energy of the single beam is redistributed into a hot spot of diameter 0.3 mm, intensity 3×10^{15} W/cm², and the same temporal profile. Here strong self-focusing is initiated in the hot spot, causing rays from the large-diameter beam to be refracted inward toward the focus. Thus a hot spot can degrade illumination uniformity over more than its own area.

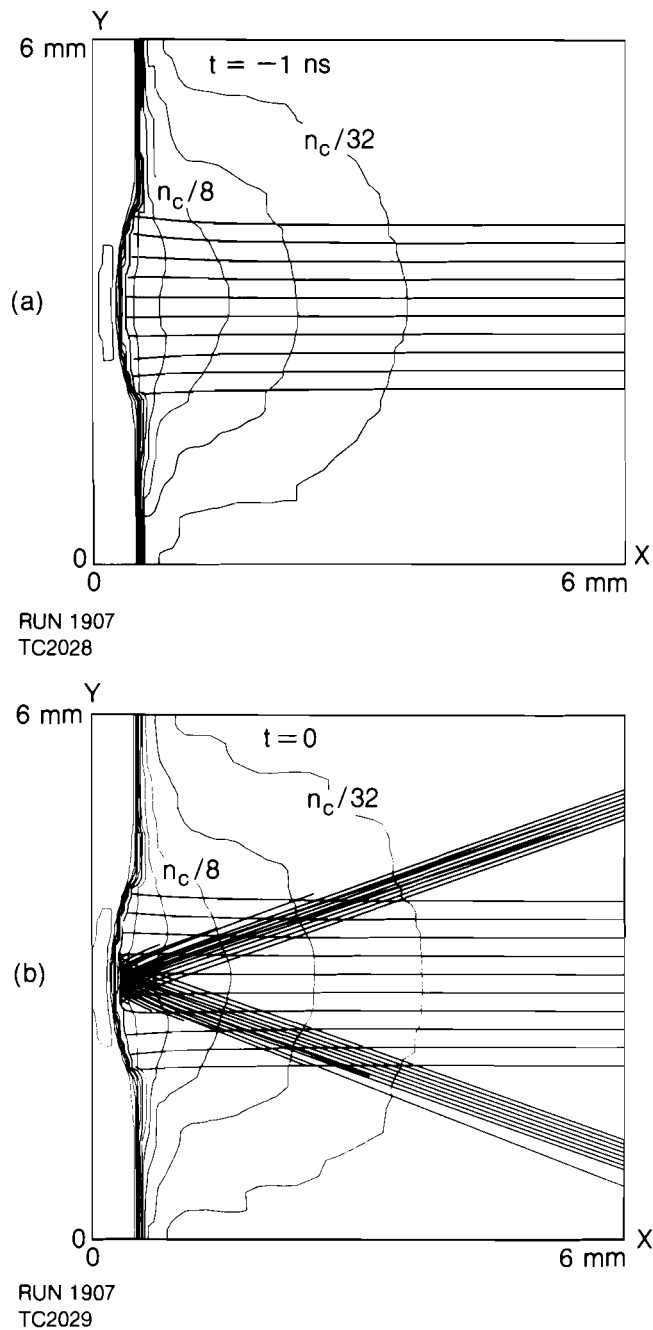


Fig. 28.17
Suppression of thermal self-focusing in a heated background plasma. Two small-diameter short-pulse beams, representing hot spots, are incident (obliquely) on a plasma produced by a large-diameter long-pulse beam of lower intensity, which might represent the early portion of a shaped reactor pulse. The coronal plasma produced by the long-pulse beam 1 ns before the onset of the short-pulse beams (a) is hardly perturbed by the time of the peak of the short-pulse beams (b).

It may be argued that these simulations are not applicable to reactor conditions, on account of the assumption of a cold preformed plasma. It is probably more realistic to consider a configuration in which the plasma is formed by a large-diameter long-pulse beam, with a small-diameter short-pulse hot spot incident upon the plasma after some time delay. Results from such a simulation are shown in Fig. 28.17, where two overlapping hot spots are used to interact with the long-scale-length plasma. Here a 10-ns beam of diameter 1.6 mm and intensity 6×10^{14} W/cm² forms a CH plasma of scale length ~ 1 mm below quarter-critical and with a coronal temperature ~ 3 keV, just before the onset of the hot spots [Fig. 28.17(a)]. The additional beams, of intensity 4×10^{15} W/cm², duration 1 ns, and diameter 0.3 mm, represent large-amplitude intensity perturbations and are synchronized to the peak of the 10-ns beam. The plasma appears to be perturbed very little by these hot spots [Fig. 28.17(a)], confirming the expectation that thermal self-focusing is less important for hot plasmas. This result is independent of whether the hot spots are incident normally or obliquely.

Summary

In the presence of overlapping laser beams, transient self-focusing effects occur in which the density perturbation of one beam affects the ray trajectories of another. Thermal self-focusing is probably not important for hot reactor plasmas, at least for the low-Z materials we have modeled, but the process may well be of concern for any target designs that result in the generation of a relatively cold long-scale-length plasma early in the laser pulse.

ACKNOWLEDGMENT

This work was supported by the U.S. Department of Energy Office of Inertial Fusion under agreement No. DE-FC08-85DP40200 and by the Laser Fusion Feasibility Project at the Laboratory for Laser Energetics, which has the following sponsors: Empire State Electric Energy Research Corporation, General Electric Company, New York State Energy Research and Development Authority, Ontario Hydro, Southern California Edison Company, and the University of Rochester. Such support does not imply endorsement of the content by any of the above parties.

REFERENCES

1. R. S. Craxton and R. L. McCrory, *J. Appl. Phys.* **56**, 108 (1984). See also LLE Review **18**, 72 (1984).
2. R. S. Craxton and R. L. McCrory, Laboratory for Laser Energetics Reports 99 and 108 (1980).
3. B. I. Cohen and C. E. Max, *Phys. Fluids* **22**, 1115 (1979).
4. M. J. Herbst et al., NRL Memorandum Report 4983 (1982).
5. L. Spitzer and R. Härm, *Phys. Rev.* **89**, 977 (1953).
6. S. P. Obenschain et al., *Phys. Rev. Lett.* **56**, 2807 (1986).
7. R. C. Malone, R. L. McCrory, and R. L. Morse, *Phys. Rev. Lett.* **34**, 721 (1975).

2.E Multiple X-Ray Diffraction in Crystals: Application to Two-Dimensional Imaging and Low-Loss Transmission

Applications of multiple x-ray diffraction in crystals was the subject of a proposal to the National Laser Users Facility by Professor Ben Post of the Polytechnic Institute of New York, in collaboration with LLE. Some results of the ensuing work are described here.

The major goals of this investigation were (a) the development of a method for two-dimensional imaging of x rays using simultaneous n-beam diffraction within crystals, and (b) the application of the above to the study of the stability of laser-irradiated spherical targets by imaging x-ray line emission from thin metallic layers embedded within plastic shell targets. We have used such diffraction to image test objects and to demonstrate the possibility of achieving satisfactory spatial resolution; these techniques will be used to image target emission.

In addition to imaging, simultaneous diffraction of x rays within crystals makes possible other applications. One involves the substantial reduction of x-ray absorption along directions that satisfy diffraction conditions with respect to several sets of crystal planes. We have demonstrated such reduction in absorption for various cases of simultaneous diffraction in germanium. Such reduction can be crucial for the successful operation of a gamma-ray laser.

Monochromatic Imaging Using Simultaneous Diffraction of X Rays by Crystals

One-dimensional imaging in the direction of dispersion is always obtained in Bragg diffraction from plane crystals. The spatial resolution (i.e., the minimum resolvable element Δx) is obtained by differentiating the Bragg equation, in first order:

$$2d\sin\theta = \lambda, \quad (1)$$

to obtain

$$2d\cos\theta\Delta\theta = \Delta\lambda. \quad (2)$$

Since the resolvable element Δx is related to the angular spread $\Delta\theta$ through $\Delta x = L\Delta\theta$, where L is the total distance traveled by the diffracted beam from the source to the detector, therefore

$$\Delta x = L \operatorname{tg}\theta(\Delta\lambda/\lambda). \quad (3)$$

In typical laser-target experiments, this spatial resolution is in fact limited by the spectral width rather than by the crystal properties. As a typical

example, we select the Ti^{+20} resonance line at 2.62 \AA and assume the laser plasma source to have an ion temperature of 1 keV. The line width will be mostly due to the Doppler effect (with some additional opacity broadening possible), so that $\Delta\lambda/\lambda = 3.5 \times 10^{-4}$, yielding a spatial resolution of $20 \mu\text{m}$ at $L = 10 \text{ cm}$. In a direction perpendicular to that of the dispersion there is no imaging at all, and the diffracted beam from a divergent source has the shape of a thin cone for a given wavelength.

Simultaneous diffraction, by contrast, can provide two-dimensional imaging.¹ The principles of simultaneous diffraction are described in Fig. 28.18. For a monochromatic incident beam, θ is adjusted to the Bragg angle for diffraction from the planes parallel to the surface. If the crystal is rotated around the ϕ axis, diffraction peaks are generated (as shown in Fig. 28.19), even when the primary reflection has zero

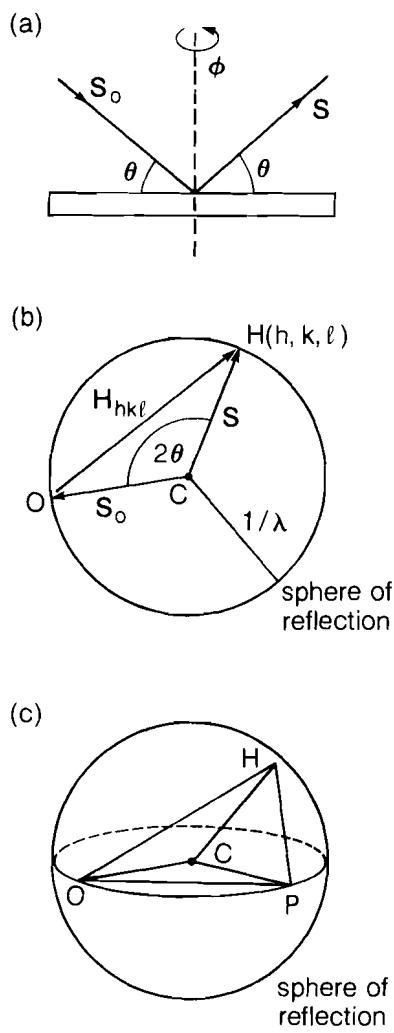


Fig. 28.18
Schematic of simultaneous diffraction:
(a) monochromatic incident beam, in
which θ is adjusted to the Bragg angle of
diffraction from the planes parallel to the
surface, and the ϕ rotation brings multiple
diffraction peaks into diffraction,
(b) Bragg condition in reciprocal lattice,
(c) by rotating around OH [ϕ -rotation in
(a)], additional reciprocal lattice points like
 P touch the reflection sphere.

intensity. To understand this, we look at the reciprocal-lattice construction [Fig. 28.18(b)]. \mathbf{S}_0 and \mathbf{S} are unit vectors in the direction of the incident and diffracted beams, respectively, and θ is the Bragg angle. The Bragg condition is satisfied when the point H lies on the sphere of reflection (the Ewald sphere): diffraction from the planes of Miller indices $(hk\ell)$ will then occur along the \mathbf{S} direction. Rotation of the crystal about the ϕ axis is equivalent to rotating the reciprocal lattice about OH [Fig. 28.18(b)]. During this rotation, many points [such as P in Fig. 28.18(c)] cross the surface of the sphere of reflection and give rise to n-beam diffraction. More than one point can simultaneously cross the surface, giving rise to higher-order n-beam diffraction (e.g., six-beam diffraction). We may say that the incident beam CO in Fig. 28.18(c) is diffracted by the OP planes (i.e., those with Miller indices equal to the coordinates of P), giving rise to a diffracted beam in the CP direction. This beam is also diffracted by the PH planes that are perpendicular to PH and are spaced $1/|HP|$ apart. These yield diffraction in the CH direction. Diffraction is in the same direction (CH) as if diffracted from the planes parallel to the surface (OH). Of course, these two diffractions are simultaneous rather than sequential.

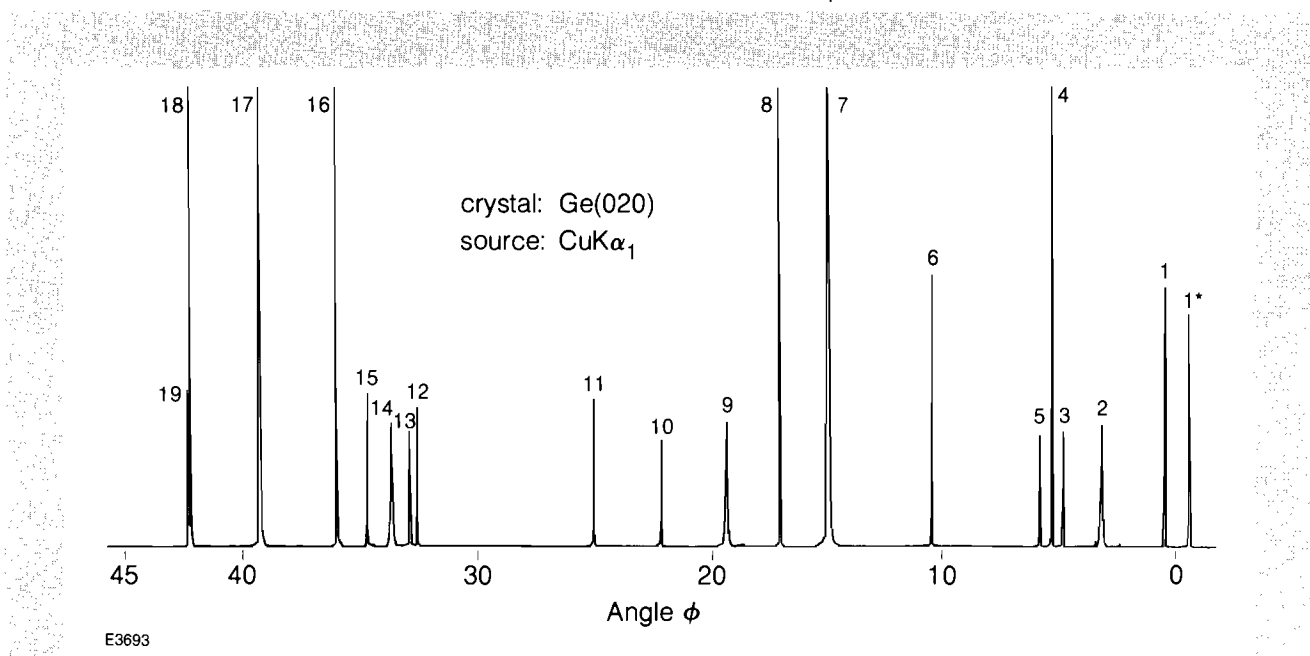


Fig. 28.19
Simultaneous (three-beam) diffraction from the (020) planes of germanium. Source: $K\alpha_1$ line of Cu.

Because two angular conditions (θ and ϕ) have to be satisfied, the diffracted beam is quasi-collimated. It can therefore yield a two-dimensional shadowgraph image, of unit magnification, of any object it traverses or of the emitting object itself. It should be emphasized that multiple diffraction is not limited to the case of zero-structure factor. In the general case, two sets of spectra can appear on the film, with the intersections, enhanced in intensity, corresponding to simultaneous diffraction. The two-beam spectra in this case constitute a background for the n-beam diffraction peaks.

Figure 28.19 shows multiple diffraction spectra obtained with $\text{CuK}\alpha_1$ radiation from an x-ray tube. The angle $\phi = 0$ is chosen so that the spectra are mirror imaged with respect to this point. Some of the peaks extend beyond the height of the figure and are truncated. The peak marked 7 in Fig. 28.19 was chosen for the imaging tests in Figs. 28.20 and 28.21; it corresponds to simultaneous diffraction from the $(1\bar{3}\bar{1})$ and $(1\bar{1}1)$ planes. The three indices add up to (020) . This simply follows from the vector relation $\mathbf{OH} = \mathbf{OP} + \mathbf{PH}$ in Fig. 28.18(c).

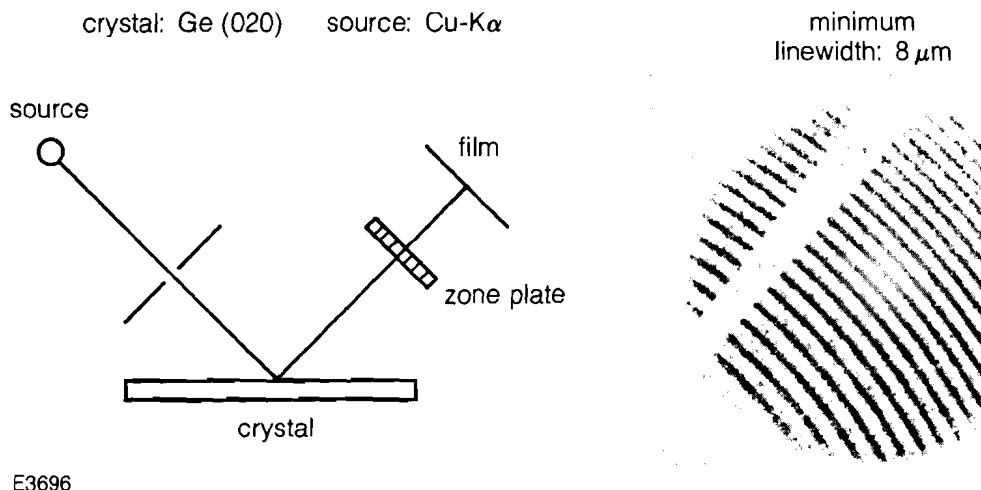


Fig. 28.20
Imaging testing using the simultaneous diffraction peak marked 7 in Fig. 28.19, from Ge (020) planes.
A weak and shifted image from the $K\alpha_2$ line can be seen.

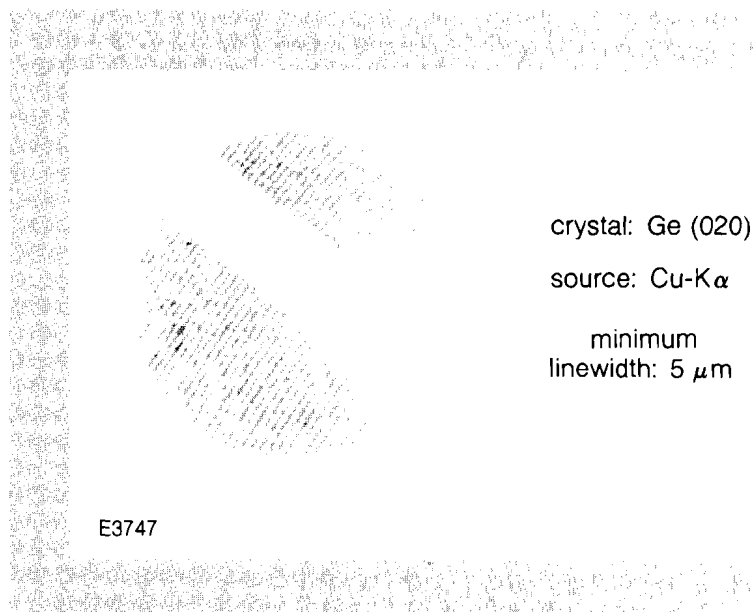


Fig. 28.21
Imaging of a finer-line section of the zone plate, as in Fig. 28.20.

Table 28.III shows the diffracting-plane indices corresponding to the scans in Fig. 28.19. The indices hkl refer to the reciprocal lattice point that passes through the surface of the Ewald sphere during rotation of the crystal. In four-beam cases, two points pass through the surface simultaneously; three points pass in five-beam cases. Azimuthal angle is the angle (relative to some arbitrary standard, such as a mirror plane) at which the point enters or leaves the sphere. Beta is the angular

Table 28.III
Simultaneous n -beam diffraction peaks: Ge (020), $CuK\alpha_1$

	$hkl(1)$	$hkl(2)$	No. of Beams	Azimuthal Angle	Beta	Azimuthal Angle
1.	$\bar{3}1\bar{3}$	$\bar{3}\bar{3}\bar{3}$	4	0.395	-90.79	269.61
2.	$\bar{1}\bar{1}\bar{7}$	---	3	2.42	-21.09	341.32
3.	$3\bar{1}\bar{5}$	$3\bar{3}\bar{5}$	4	5.15	51.62	56.78
4.	$3\bar{1}\bar{1}$	---	3	5.38	132.37	137.75
5.	$\bar{3}\bar{1}\bar{5}$	---	3	5.63	-73.18	292.44
6.	$\bar{3}\bar{1}\bar{3}$	---	3	10.36	-110.71	259.64
7.	$\bar{1}\bar{3}\bar{1}$	$\bar{1}\bar{1}\bar{1}$	4	14.90	-119.79	255.11
8.	$3\bar{1}\bar{1}$	$3\bar{3}\bar{1}$	4	17.24	108.65	125.89
9.	$1\bar{1}\bar{7}$	---	3	18.68	-21.09	357.58
10.	$5\bar{1}\bar{3}$	---	3	22.44	73.18	95.63
11.	$\bar{1}\bar{3}\bar{5}$	$\bar{1}\bar{1}\bar{5}$	4	24.90	-72.42	312.48
12.	$5\bar{1}\bar{1}$	---	3	32.76	91.85	124.62
13.	$5\bar{1}\bar{3}$	$5\bar{3}\bar{3}$	4	33.22	51.62	84.85
14.	$5\bar{1}\bar{5}$	---	3	34.45	21.09	55.55
15.	$\bar{1}\bar{1}\bar{5}$	---	3	34.62	-91.85	302.76
16.	$\bar{1}\bar{3}\bar{3}$	$\bar{1}\bar{1}\bar{3}$	4	35.89	-108.65	287.24
17.	$\bar{1}\bar{1}\bar{1}$	---	3	39.24	-168.49	230.76
18.	$3\bar{1}\bar{1}$	---	3	42.25	132.37	174.62
19.	$5\bar{3}\bar{1}$	$5\bar{1}\bar{1}$	4	42.48	72.42	114.90

Diffraction peaks obtained when rotating the crystal around the normal to the (020) planes. The Bragg angle with respect to these planes is maintained while the azimuthal angle changes. For each diffraction peak, the table shows the coordinates of the reciprocal lattice point(s) whose passage through the surface of the sphere of reflection gives rise to that peak. The two azimuthal angles correspond to either entering or leaving the reflection sphere. Beta is the difference between these two angles. For negative beta, the first angle corresponds to exit; for positive beta, it corresponds to entry.

interval between entry and exit of the sphere. If beta is negative, the first azimuthal angle (in column 4) refers to emergence from the sphere, and the second azimuthal angle (in column 6) to entry; if beta is positive, the above are reversed.

Figures 28.20 and 28.21 show imaging test results obtained with CuK α radiation. A freestanding gold zone plate was chosen as a test object to be imaged by shadowgraphy onto a high-resolution film (Kodak RAR-2497). The 0.5-mm pinhole limits the image size and reduces some background, but has no effect on the imaging. The smallest zone plate linewidth in Fig. 28.20 is 8 μm , and in Fig. 28.21 it is 5 μm . This is an indication of the spatial resolution achievable in a direction perpendicular to that of the dispersion. In these figures, the distance of source to zone plate (along the ray) is 200 cm, and that of the zone plate to film is 2 cm. The source size is about 3 mm, yielding a penumbral shadow of at least 30 μm . Clearly, the imaging in these figures is due to the properties of simultaneous diffraction.

The direction of dispersion is seen in Fig. 28.20, as the K α_2 component gives rise to a weak, shifted image with respect to the dominant image. In this direction the spatial resolution is limited by the spectral linewidth, just as in two-beam Bragg diffraction. As shown above, at a total distance of 10 cm this resolution will be typically 20 μm . In the perpendicular direction the spatial resolution can only be limited by the crystal properties. For the germanium crystal used, the rocking-curve width is about 10^{-4} , yielding a spatial resolution of 2 μm for the 2-cm imaging distance in Fig. 28.20. This agrees with Fig. 28.21, which indicates a resolution better than 5 μm . In this case, the zone plate was rotated by about 90°, to demonstrate the resolution perpendicular to the direction of dispersion. For a total distance of 10 cm from a laser target to the crystal, then to the film, a 10- μm resolution can be achieved in this direction. Different wavelengths will yield images displaced with respect to each other. As shown here, 10- μm to 20- μm resolution is possible in a two-dimensional image at each wavelength. Such images can be useful in studying instability and mixing in laser target implosions. For this, thin layers of elements like titanium or chromium have to be embedded in the target and isolated, strong x-ray lines from the various layers have to be imaged.

Reduction in Absorption on Multiple-Diffraction Beams

Simultaneous diffraction has other important applications, in addition to imaging:

- (a) In the Laue mode (radiation traversing the crystal), absorption due to the photoelectric effect is greatly reduced² for n-beam diffraction peaks. This is in addition to the reduction in absorption (Borrmann effect) in all two-beam, Laue diffraction. This property is important for designs of gamma-ray lasers where propagation of wavelengths of order 1 Å through a relatively large thickness of crystalline material is called for.
- (b) The spectral dispersion in this case has two components: $d\theta/d\lambda$ and $d\phi/d\lambda$. The second dispersion can be much larger than the first, yielding a high-resolution recording of spectra.

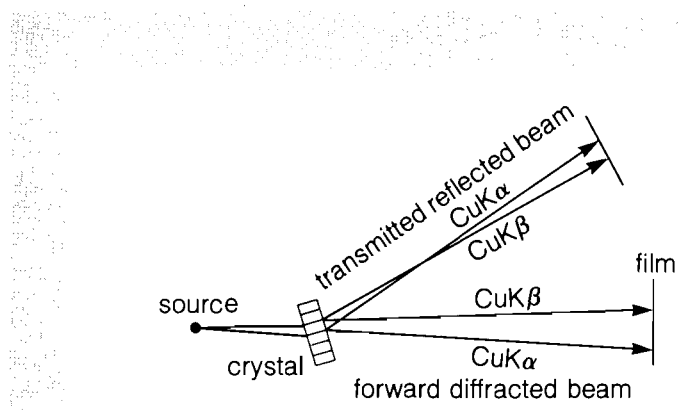
- (c) The profiles of n-beam diffraction peaks near the baseline indicate the sign of the phase shift introduced by the diffraction, thereby making possible the experimental determination of x-ray reflection phases from diffraction data.³

The multiple diffraction described above was measured in reflection (or Bragg diffraction), whereas the reduction in absorption described here was measured in transmission (or Laue diffraction). The principles of resonant x-ray beams in crystals (i.e., multiple diffraction) are essentially the same in both cases. However, for the determination of absorption the transmission case is the more relevant.

We show in Fig. 28.22 the geometry used in the Laue case. In the measurements leading to Fig. 28.19, the crystal had to be rotated in order to scan the peaks of multiple diffraction, whereas here we used film to record simultaneously the diffracted beams in a range of directions. In Fig. 28.19 the incident beam needs to be collimated; here, we use a divergent beam, placing a micro-focus source (0.1x0.1 mm) close to the crystal (7 cm). The film is placed far from the crystal (200 cm) to increase the ratio of signal to scattered background and to avoid broadening due to the source size.

Other characteristic differences between the results obtained in this and the previous subsection will be noted. As Fig. 28.22 shows, in conventional Laue diffraction there are two beams that leave the crystal: the forward-diffracted beam, which travels in the same direction as the incident beam (except for a slight shift that depends on the crystal thickness and the Bragg angle); the transmitted-reflected beam, which is analogous to the one diffracted beam in the case of Bragg diffraction.

In the experiments described in the previous subsection, the Bragg angle with respect to the planes parallel to the crystal surface corresponded to a so-called forbidden diffraction (i.e., having a zero structure-factor). Therefore, diffracted beams were observed only in directions corresponding to multiple diffraction. In Fig. 28.22, the divergent beam can give rise to two-beam Laue diffraction, which will



E4023

Fig. 28.22
Laue (transmission) geometry for measuring multiple-diffraction peaks.

appear on film as lines in the plane of the figure. Diffracting planes other than those shown in Fig. 28.22 will yield lines in different orientations. The transmitted-reflected beam may also satisfy the diffraction condition with respect to a second set of planes. This will be evidenced by an *enhancement* at one point along the line, mainly due to the theoretically predicted reduction in absorption. For the forward-diffracted beam this point of enhancement is observed at the intersection of two lines on the film, from the two two-beam interactions.

Figures 28.23 and 28.24 show examples of results obtained with the geometry of Fig. 28.22, where radiation from a copper-anode tube is transmitted through a 0.5-mm-thick germanium crystal.

Figure 28.23 shows the enhancement due to reduction in absorption at the intersection points of pairs of forward-diffracted beams (lower right). Also, it shows n-beam enhancement points on transmitted-reflected beams (upper and left features).

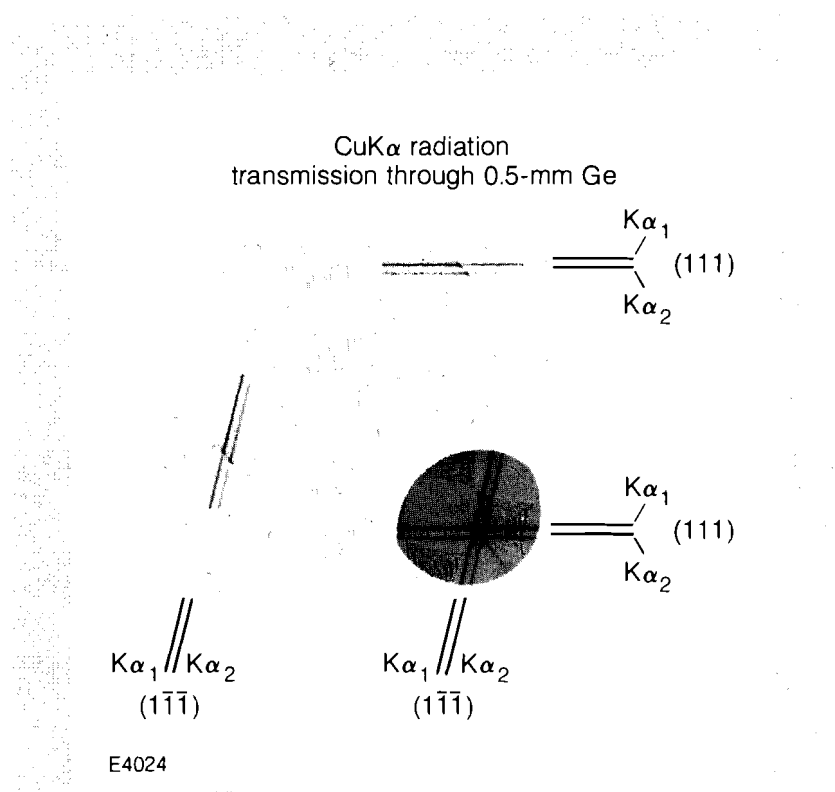


Fig. 28.23
Three-beam diffraction (at enhanced-intensity points).

Figure 28.24 shows a four-beam diffraction case, where the four reciprocal lattice points are 000 , $1\bar{1}1$, $20\bar{2}$, and $3\bar{1}\bar{1}$. The four points are coplanar. The divergent incident beam enables the observation of $3\bar{1}\bar{1}$ diffraction lines due to $CuK\alpha_1$, $K\alpha_2$, and $CuK\beta$, as well as four-beam enhancements at these wavelengths. The vertical streak that passes through the $K\alpha_1$, $K\alpha_2$, and $K\beta$ four-beam points is due to the four-beam enhancement of the very faint continuum of wavelengths between $K\alpha$ and $K\beta$. Theory shows that when a larger number of interactions

occur simultaneously, the reduction in absorption is more pronounced. In a six-beam case in germanium, the linear absorption coefficient for three of the modes (for 1.54-Å radiation) is calculated⁴ to be less than 1 cm^{-1} (there are 12 modes when polarization is included). The absorption in other modes ranges up to 690 cm^{-1} . The total attenuation through a thickness of a few millimeters should therefore be very small. A quantitative determination of these values will be the subject of continuing work.

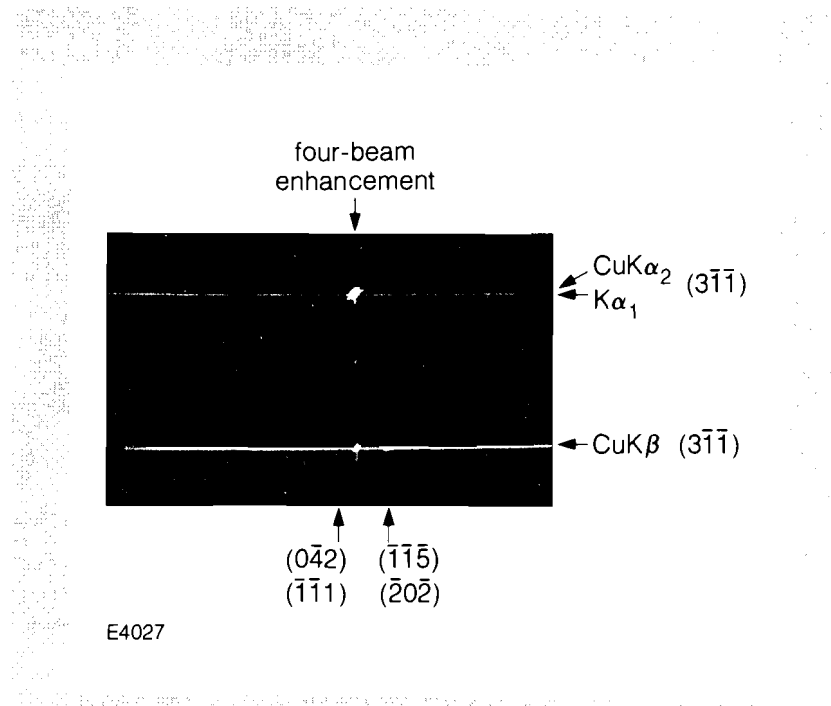


Fig. 28.24

Four-beam diffraction (at enhanced-intensity points). The vertical line is enhanced, four-beam diffraction of the continuum.

ACKNOWLEDGMENT

This work was supported by the U.S. Department of Energy Office of Inertial Fusion under agreement No. DE-A508-84DP40197 with the Polytechnic Institute of New York and by the National Laser Users Facility at the University of Rochester Laboratory for Laser Energetics under agreement No. DE-FC08-85DP40200.

REFERENCES

1. B. S. Fraenkel, *Appl. Phys. Lett.* **36**, 341 (1980); **41**, 234 (1982).
2. B. Post, S. L. Chang, and T. C. Huang, *Acta Crystallogr. Sect. A*: **33**, 90 (1977); B. Post, *ibid.* **39**, 711 (1983); B. Post, J. Nicholosi, and J. Ladell, *ibid.* **40**, 684 (1984).
3. B. Post, *Phys. Rev. Lett.* **39**, 760 (1977).
4. T. C. Huang, M. H. Tillinger, and B. Post, *Z. Naturforsch.* **28a**, 600 (1973).

Section 3

ADVANCED TECHNOLOGY DEVELOPMENTS

3.A Propagation of Femtosecond Electrical Pulses on Superconducting Transmission Lines

An electro-optic sampling system has been used at LLE in the past to characterize transistors with rise times as fast as 5 ps at room temperature.¹ With devices operating at these speeds, it now becomes important to consider the details of how these very fast signals propagate. This can be seen in Fig. 28.25, where the impulse response of two types of transistors is shown.² Both responses clearly show the effects of the negative input pulse being coupled through to the output. In order to study the propagation of these very fast pulses, the sampling geometry of Fig. 28.26 was used. As shown, the LiTaO₃ and GaAs crystals were edge polished separately and then glued together to form a very well-matched interface. After surface polishing, the structure is so uniform that metal electrodes can be evaporated across the interface without discontinuities. This geometry has been used at room temperature to measure an electrical rise time of 460 fs.³

Since a superconductor exhibits an absence of dc resistivity, it was expected that a sampling structure with superconducting electrodes would show an increase in speed. In addition to requiring the ambient temperature to be less than the superconducting transition temperature, we also require that the laser pulses propagate undistorted through the experimental apparatus. This is accomplished by the use of superfluid helium, with a temperature of $\approx 2^{\circ}\text{K}$. When the temperature of liquid helium is reduced below the lambda point, all bubbling is precluded and the liquid becomes completely quiescent. An early version of the sampler, using standard Pb-In-Au alloy electrodes and wire bond

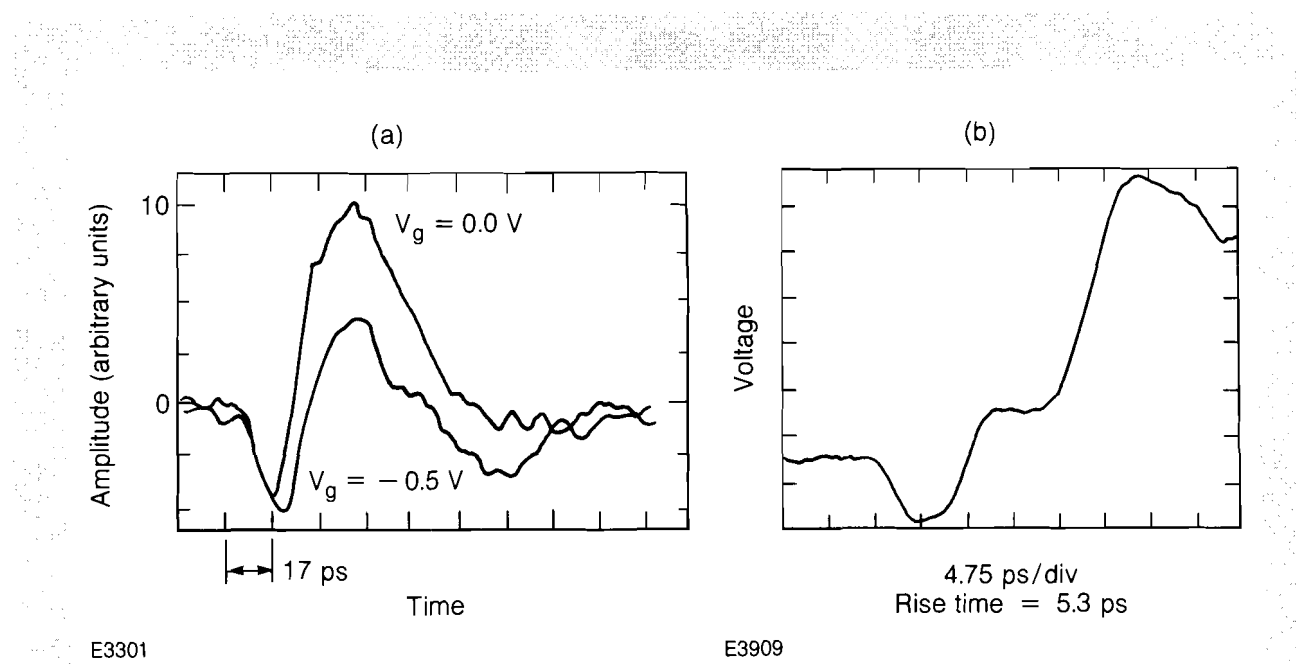


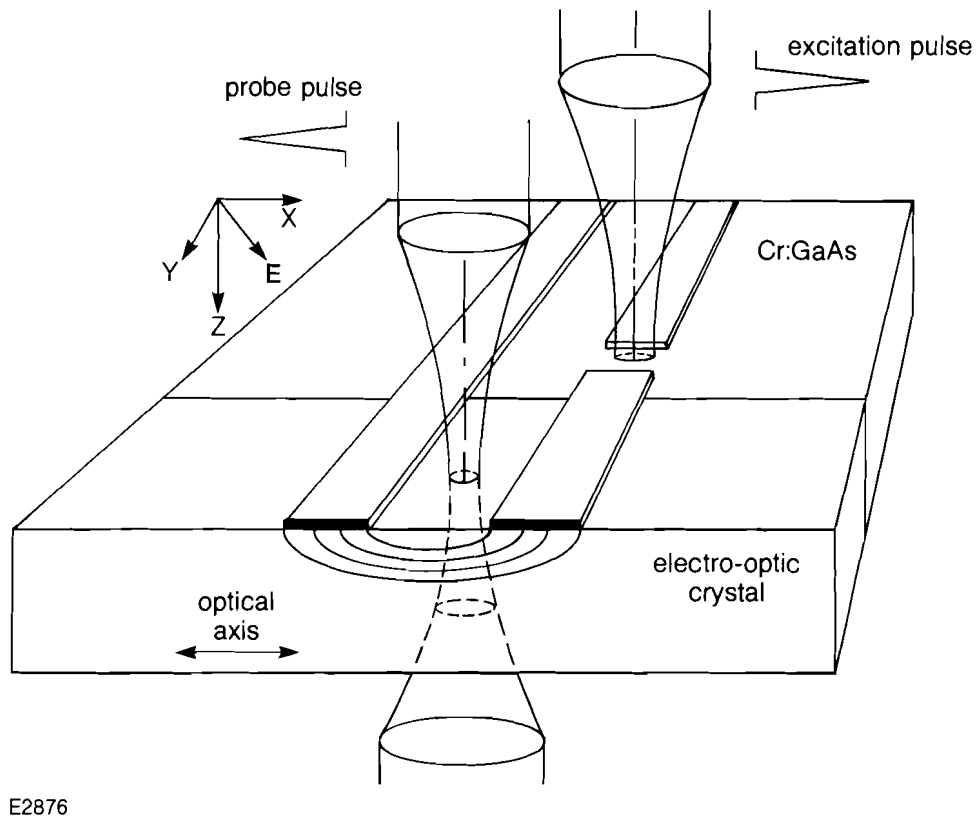
Fig. 28.25

Measured transistor step responses. Both the two-dimensional electron gas FET (a), and the permeable base transistor (b), show the effects of input-pulse coupling through to the output.

connections across the $\text{LiTaO}_3/\text{GaAs}$ interface showed a fivefold increase in performance to 1-ps rise time, when cooled down from room temperature. The temporal response for a sampler with indium electrodes is shown in Fig. 28.27. With a rise time of 360 fs, the propagation characteristics of the coplanar geometry could now be studied.

Pulse distortion can be divided into two separate components caused by frequency-dependent absorption and frequency-dependent propagation velocity, also known as modal dispersion. Frequency-dependent absorption is caused by skin effect losses inside the conductors. As the frequency increases, the skin depth decreases, and so the effective resistance (loss) becomes greater for increasing frequency.

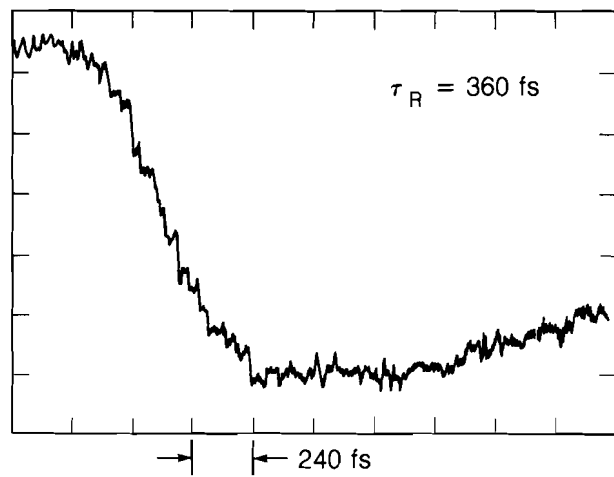
The corresponding mechanism for superconductors is somewhat different. Current is conducted in a superconductor not by electrons, called quasi particles, but by paired electrons called Cooper pairs. It is these Cooper pairs that conduct the zero-voltage current or supercurrent. Cooper pairs constitute a lower energy state than do quasi-particles, but at a high enough frequency these Cooper pairs are broken. This frequency is a material-dependent parameter, related to the energy gap by $E = h\nu$. For indium the energy gap is 1.05 mV, corresponding to a frequency of about 250 GHz. Above this frequency, the current is conducted by quasi-particles, but because of the low ambient temperature, the losses are expected to be much reduced over the room-temperature values.



E2876

Fig. 28.26

Sampling geometry. In practice the entire structure is immersed in a superfluid helium bath. This allows undistorted laser-beam propagation into and out of the experimental dewar.



Z15

Fig. 28.27

Rise time of the indium electrode sampler.

Modal dispersion, on the other hand, is not a mechanism based on the materials used, but rather on transmission-line geometry. This effect can be minimized by using transmission lines of small cross-sectional dimension. Consider again the coplanar transmission-line geometry. The electric field propagates above and below the LiTaO_3 /superfluid helium interface. Since the relative dielectric constants are vastly different (≈ 35 versus 1.08 for the helium), the velocity of propagation will be different above and below the interface. This result can be seen for the superconducting system in Fig. 28.28. The classic features are exhibited by the fall time becoming shorter than the rise time, and by the development of the small post pulses. All of these features have been observed previously at room temperature.⁴

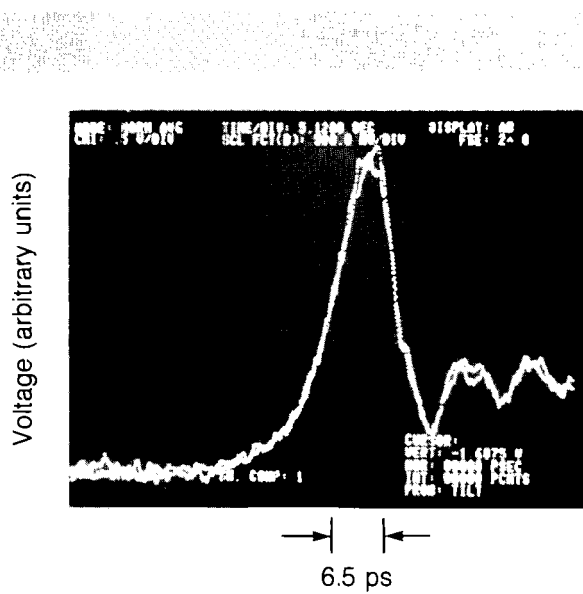


Fig. 28.28
Purely radiational electromagnetic signal demonstrating the classic signs of dispersion: rise time slower than fall time; small post pulses.

While reducing the dimensions will reduce the area of dielectric mismatch and hence reduce the effect of modal dispersion, the smaller conductor cross section will increase the conductor losses and so increase the frequency-dependent loss. Clearly, in designing a high-speed transmission system these two mechanisms must be balanced.

By measuring the rise time as a function of distance, the severity of the distortion for a particular system can be measured. Propagation measurements that were made on the electro-optic sampling system since 1982 are summarized in Fig. 28.29. The balanced stripline (curve A) shows a nearly vertical dispersion characteristic, resulting in a 9-ps rise time after 3 mm. Curve C shows results from a structure in which the dielectric mismatch between substrate and superstrate was minimized.⁵ The increase in rise time per unit length of propagation is relatively low. Finally, the results on the superconducting line show that the signal rise time increased to only 2 ps after 3 mm. The improvement in performance can be seen by comparing the superconducting result to a similar geometry at room temperature (curve B).

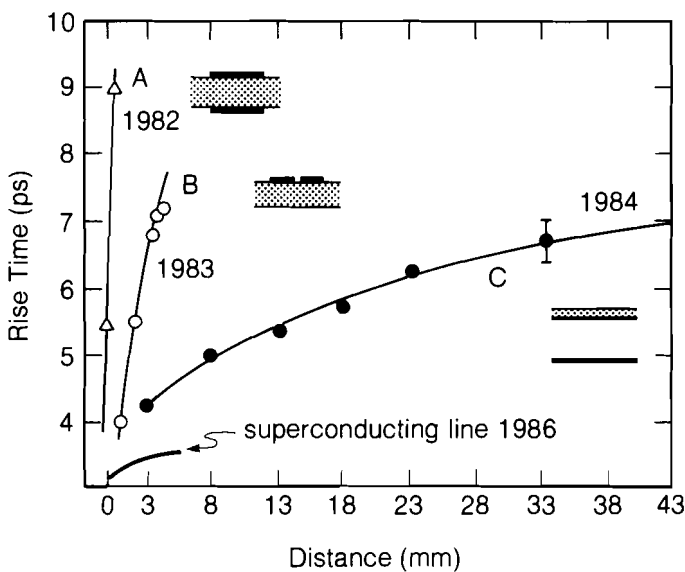


Fig. 28.29

Dispersion measurements made on the electro-optic system since 1982. The transmission-line geometry is shown in cross section, next to each curve.

In order to model these results, a computer program used previously for room-temperature pulse propagation was used.⁶ The only change made in the program was to assume that the frequency-dependent losses in the superconductor were negligible. As shown in Fig. 28.30 for a particular data set, the results are very well predicted by the purely geometry-dependent dispersion model.

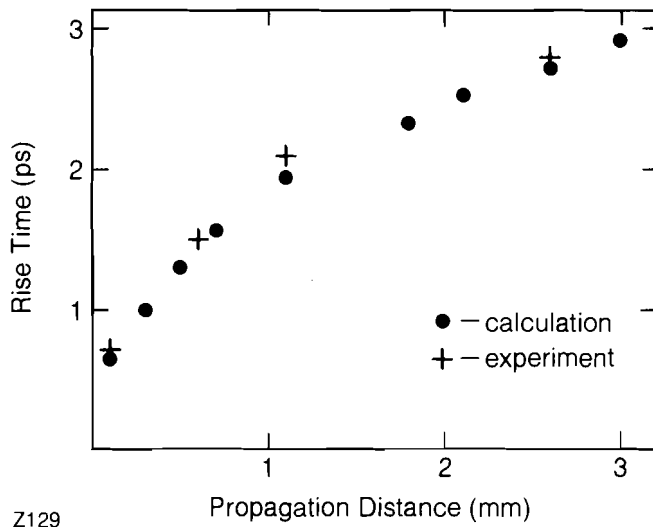


Fig. 28.30

Comparison between superconducting coplanar transmission dispersion data and computer model, using lossless approximation.

In summary, our electro-optic sampling system has been used in the cryogenic regime to characterize electrical waveforms in the THz frequency range. The system has been used to study pulse propagation on superconducting transmission lines where a rise time of 360 fs was measured, dispersing to only 2 ps after 3 mm of propagation. This very significant improvement in dispersion was due to the use of superconducting electrodes, which allowed the effects of modal dispersion to be minimized while still providing for very low-loss signal conduction. Finally, these results were modeled by considering a lossless case for modal dispersion.

ACKNOWLEDGMENT

This work was supported by the National Science Foundation under agreement No. DMR-8506689 and by the Laser Fusion Feasibility Project at the Laboratory for Laser Energetics, which has the following sponsors: Empire State Electric Energy Research Corporation, General Electric Company, New York State Energy Research and Development Authority, Ontario Hydro, Southern California Edison Company, and the University of Rochester.

REFERENCES

1. D. R. Dykaar, G. A. Mourou, M. A. Hollis, B. J. Clifton, K. B. Nichols, C. O. Bozler, and R. A. Murphy, *Proceedings of the Conference on Lasers and Electro-Optics*, 9–13 June 1986, San Francisco, CA, (OSA/IEEE, 1986), p. 314.
2. K. E. Meyer, D. R. Dykaar, and G. A. Mourou, in *Picosecond Electronics and Opto-electronics*, edited by G. A. Mourou, D. M. Bloom, and C. H. Lee (Springer-Verlag, Berlin, Heidelberg, New York, and Tokyo, 1985), p. 54.
3. G. A. Mourou and K. E. Meyer, *Appl. Phys. Lett.* **45**, 492 (1984).
4. J. A. Valdmanis and G. A. Mourou, *IEEE J. Quantum. Electron.* **QE-22**, 69 (1986).
5. C. J. Kryzak, K. E. Meyer, and G. A. Mourou, in *Picosecond Electronics and Opto-electronics*, edited by G. A. Mourou, D. M. Bloom, and C. H. Lee (Springer-Verlag, Berlin, Heidelberg, New York, and Tokyo, 1985), p. 54.
6. J. F. Whitaker, T. B. Norris, G. A. Mourou, and T. Y. Hsiang, to be published in *IEEE Trans. Microwave Theory Tech.* **MTT-35** (January 1987).

3.B The Image Analysis Laboratory Facility for Processing Film Data

Film continues to be the most versatile medium used in the Laboratory for recording spectra and images over a wide range of wavelengths from infrared to x rays. No other recording medium or device has the sensitivity, resolution, and dynamic range of photographic film. The Image Analysis Laboratory was formed two years ago to develop facilities for both routine digitization, reduction, analysis, and presentation of film-based data, as well as the continued development of new techniques and procedures. During the past year these capabilities have been realized and used by a variety of staff members and outside users.

Facilities

The facilities include a Perkin-Elmer 1010G microdensitometer (PDS), which is routinely used to scan film ranging in size from 20-cm-diameter laser near-field images, scanned with a 400- μm aperture, to 5-mm 2 x-ray pinhole photographs scanned with a 20- μm aperture. The instrument is mounted on a granite base for stability, and weighs nearly 2,000 pounds (Fig. 28.31). It passes a narrow beam of light through the film,



Fig. 28.31
The Perkin-Elmer 1010G microdensitometer (PDS).

CR88

which is restrained between two glass platens. The platens are moved in both x and y directions, allowing a computer to scan the film mechanically and digitize the analog output of a photomultiplier tube (PMT). This is a 12-bit conversion allowing an accuracy of one part in 4096 of film densities from 0.0 to 5.1. It is interfaced via a parallel direct-memory access port to a scientific workstation.

The three computers used in the Image Analysis Laboratory are scientific workstations manufactured by Sun Microsystems (Fig. 28.32). These computers are connected via a 10 megabit/second *ethernet* network, and they have high-resolution (approximately 1000 × 1000 points) black-and-white screens, used for the display of graphics and images. These computers run the UNIX¹ operating system. The majority of the image-processing codes are written in either the C or FORTRAN programming languages. Additional available programming languages include Mongo (a graphics language developed at MIT and adapted for use at LLE), Magic/L, Forth, Lex, Yacc, and Pascal. All source codes are organized under a facility known as RCS (Resource Control System), which allows access to and control of earlier revisions of programs under development.

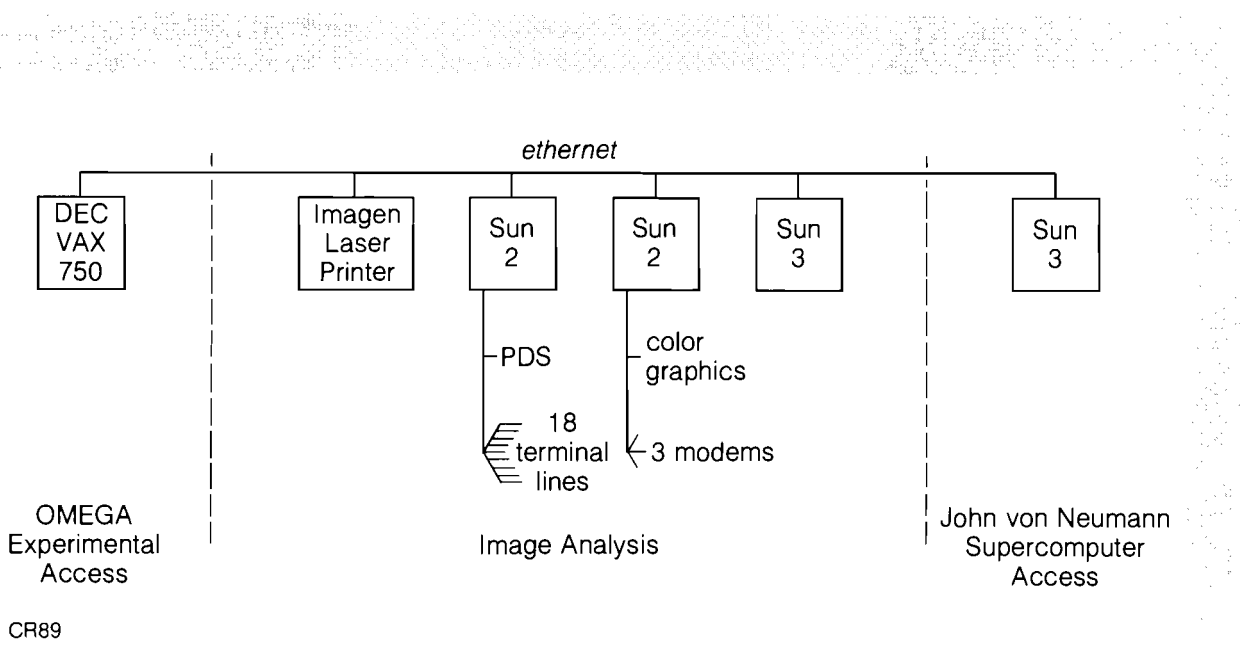


Fig. 28.32
The Image Analysis Laboratory computer network.

Each of these computers has either a 10-MHz Motorola 68010 or 16.67-MHz 68020 processor and 4 megabytes of main memory, with over 1 billion bytes of disk storage distributed among them. The Sun Microsystems Network File System (NFS) allows access to programs and data by file name, regardless of which machine the files are stored upon. As a result, programs, data files, and disk drives can be organized to process images most efficiently. Currently, 310 megabytes of storage are available for images, 315 megabytes for image processing codes and documentation, and 512 megabytes for the UNIX system, its source code, and backups.

These computers are also accessible from conventional terminals via 9600-baud (bits/second) RS-232 lines. In addition, users of the National Laser Users Facility (NLUF) have accessed the facilities remotely via a 1200-baud telephone connection. The facility is part of a larger Laboratory *ethernet* network that includes a Digital Equipment VAX 750 computer, used for experimental data acquisition, archiving, and reduction, and the LLE/John von Neumann Center Graphics workstation, which is also a Sun-3 system. In addition, there is access to other outside laboratories and universities via the Usenet and Arpanet networks.

Graphic and image output is provided by a variety of means. Graphics and images may be presented on the CRT's of the two workstations, and most graphics terminals are also supported. However, high quality images may be viewed with a moderate resolution color/gray-scale CRT (480 x 640 pixels). This resolution is adequate for the majority of image data. Hardcopy can be provided by multipen plotters, a Dunn color CRT hardcopy device using either 35-mm or Polaroid film backs, or an Imagen laser printer with 300 dots/inch resolution. Each of these graphic-output devices has been dimensionally calibrated to allow direct measurements of the data. These facilities and computer codes are maintained by a system administrator responsible for the UNIX system and the computer network, an applications programmer often assigned to a specific project, and several students.

Table 28.IV
Image-processing codes

<i>contour</i>	plots an isointensity or isodensity image with optional shading
<i>convolve</i>	convolves an image with an n x m kernel
<i>dlogI</i>	computes D-logI curves
<i>display</i>	displays images to a variety of output devices
<i>FFT</i>	computes Fast Fourier Transform
<i>iconvert</i>	intensity corrects an image
<i>histo</i>	plots a variety of frequency/intensity histograms
<i>plot-ical</i>	plots an intensity calibration curve
<i>plot-scan</i>	plots a single scan line
<i>scanregion</i>	acquires a digitized image from the PDS microdensitometer
<i>smooth</i>	smooths an image
<i>window</i>	takes a subset of an image
<i>zoom</i>	shrinks an image

CR92

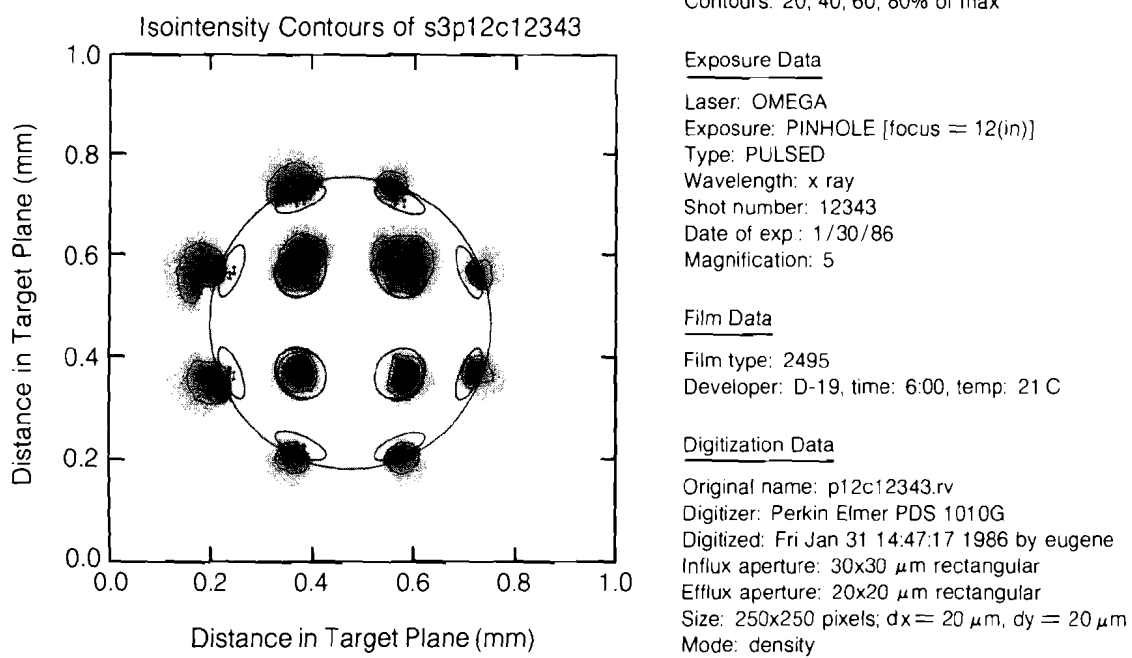
System Software

As shown in Table 28.IV, a variety of computer codes have been developed. The majority of these programs can be operated either from a menu system or by typing a single command with parameters. For example, the *contour* routine produced the contour of an intensity-corrected x-ray pinhole picture shown in Fig. 28.33.

The title may specify either isodensity or isointensity contours. The X and Y axes may be labeled in either millimeters or microns, as appropriate, and specify image or target planes, as selected. If shading is present, as it is here, then a shading key will indicate levels either as a percent of highest intensity or as a density value. The subheader information shows what program produced this plot, in this case *contour.run*, with various options passed to the program, including the file name. It also indicates the sampling aperture, the pixel size, the magnification, the peak density, and the contour levels selected.

Fig. 28.33

X-ray pointing shot on OMEGA with precalculated beam positions.



It is necessary to maintain a history of processing steps an image undergoes. This is accomplished in two ways. First, the image file name has prefixes added for each processing step. In the case of Fig. 28.33, the file name is *s3p12c12343.rv*. Here *s3* shows that the image was smoothed, averaging over three points at a time. An *i* would have indicated that the data had been intensity converted, and a *z*, followed by a number, would have shown that it had been zoomed, or demagnified, by that factor. *P12c* indicates that this was taken from the third image from the 12-in. x-ray pinhole camera. The data was taken on the OMEGA shot No. 12343. Finally, *rv* indicates that this is an image file name (*rv* for Rochester Vision, a format developed by the University of Rochester computer science department). Additionally, a data header and multiple subheaders maintain computer-readable information on the exposure, digitizing, and processing steps.

Operation

One of the major processing difficulties is in calibrating the film response. Methods have been developed to relate film density to source irradiance. In some cases, as with x-ray film, a mathematical formula can be used² to calculate this relationship. In other cases, a step wedge of known densities is exposed on the film with the data, and later digitized to produce a relative D-logI curve. In the next section an alternative method for producing such a curve will be examined.

Equally important, film processing must be handled under controlled conditions. A JOBO ATL-1 automatic film processor assists with this by developing film for known periods of time with the temperature controlled to within a few tenths of a degree. An automatic film processor also gives complete control over the use of developing chemicals and, since the film processor is sparing in its use of reagents, developing chemicals are not reused.

The film is then digitized on the PDS using the *Scan-Region* program. Scanning takes from a few minutes to several hours, depending upon the aperture and the area to be scanned. Smaller apertures result in a larger number of samples per unit area and also require slower scanning times because of the reduced light reaching the PMT in the microdensitometer. If a step wedge was taken with the data, it will be scanned separately and stored in a calibrated file.

At this step, some images are converted to intensity with the *Iconvert* program, via a table-lookup. Other processing steps include making a series of intensity histograms, which give the distribution of intensities in an image. Some data are subjected to Fourier analysis, as well as a variety of user programs such as calculating the center and radius of x-ray pinhole pictures.

Users have the option of keeping their data on disk or copying it to magnetic tape. If data are left on disk, they are eventually archived on tape and removed from disk to save space. The disposition of a particular archived file is maintained on a computer so that it can be restored.

Calibrating IR and UV Film

One of two major uses of this facility is in support of the laser uniformity program.³ The goal is to increase the uniformity of the energy distribution across each OMEGA beam. Analysis of both near-field and far-field laser distributions are made, leading to the identification of beam perturbations and their eventual removal.

However, there are neither standard sources nor step-wedges for either IR or UV film calibrations. As a result, a technique has been developed to calibrate these types of film using lasers of the appropriate wavelengths. The experimental setup in Fig. 28.34 is used for calibration of IR film; a similar setup is used for calibrating UV film, using an argon ion laser. An etalon, or rattle plate, gives spatially distinct exposures, labeled A, B, C, and D, each having a known, and decreasing, percentage of the incident laser energy.

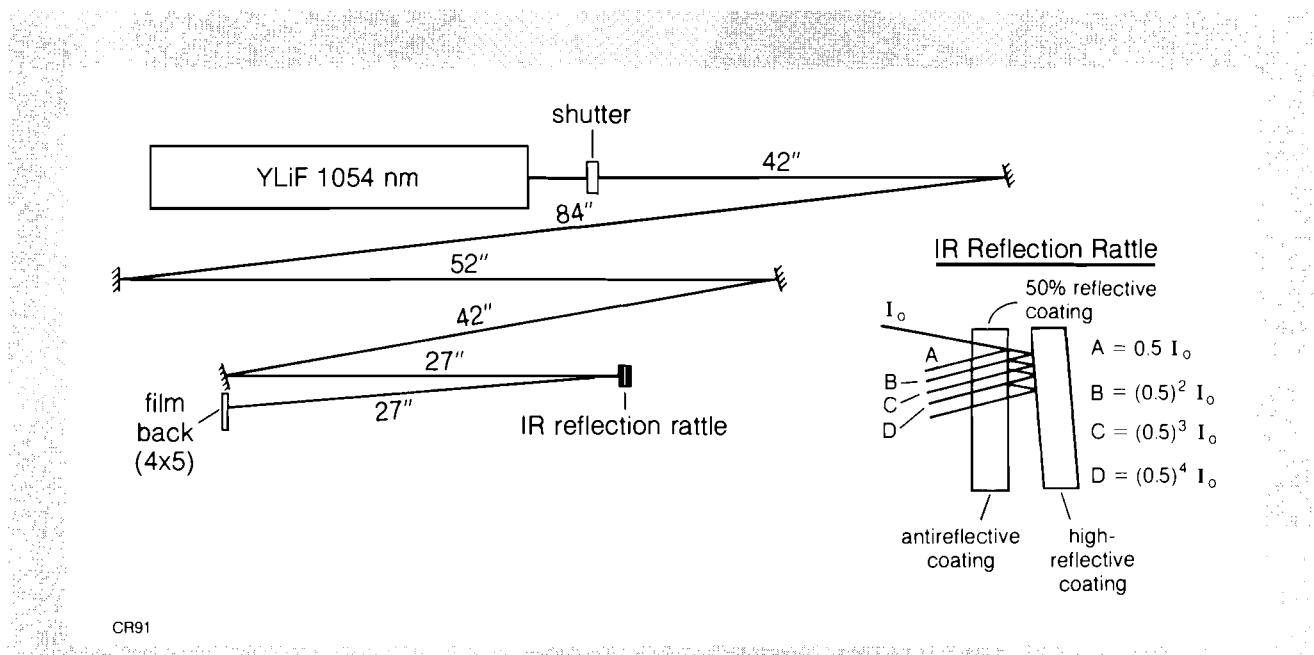


Fig. 28.34
Setup for calibrating IR films.

Two adjacent exposures are then digitized. Although these two exposures cannot be directly compared, an indirect method provides a means of establishing the calibration curve. First, a cumulative density histogram is calculated similar to the reversed cumulative histogram (since we wish to begin with the peak density) shown in Fig. 28.35. If two points are selected at the same height on the graph, their respective irradiances differ by a factor of 2 [such as A1 and B1, or A2 and B2 in Fig. 28.35(a)]. This process can be repeated, eventually resulting in a relative calibration curve, as shown in Fig. 28.35(b).

Processing Experimental Results

The other major use of this facility is to support a variety of imaging and spectroscopic instruments on OMEGA and GDL. X-ray pinhole pictures are often used as indicators of laser irradiation uniformity and are compared directly with theoretical calculations. For example, a user

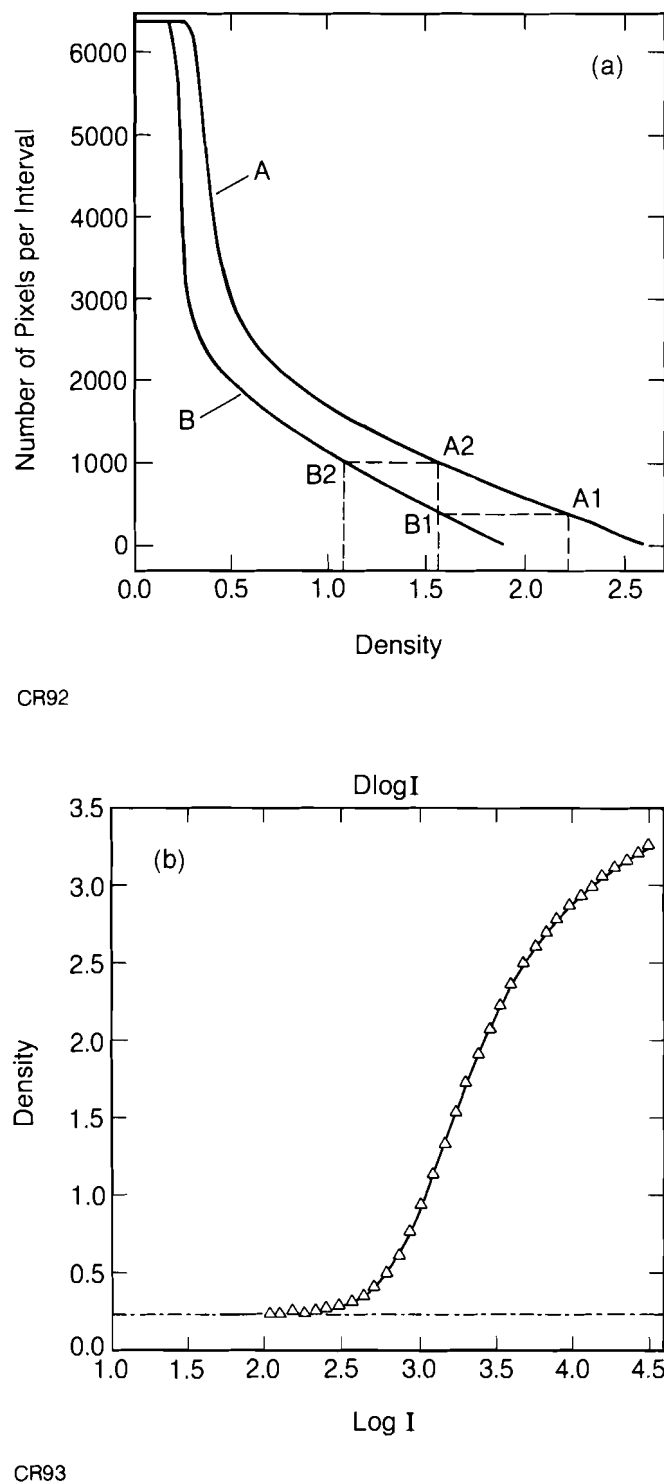


Fig. 28.35
 (a) Reverse cumulative density histogram.
 (b) $D\text{-}log I$ curve.

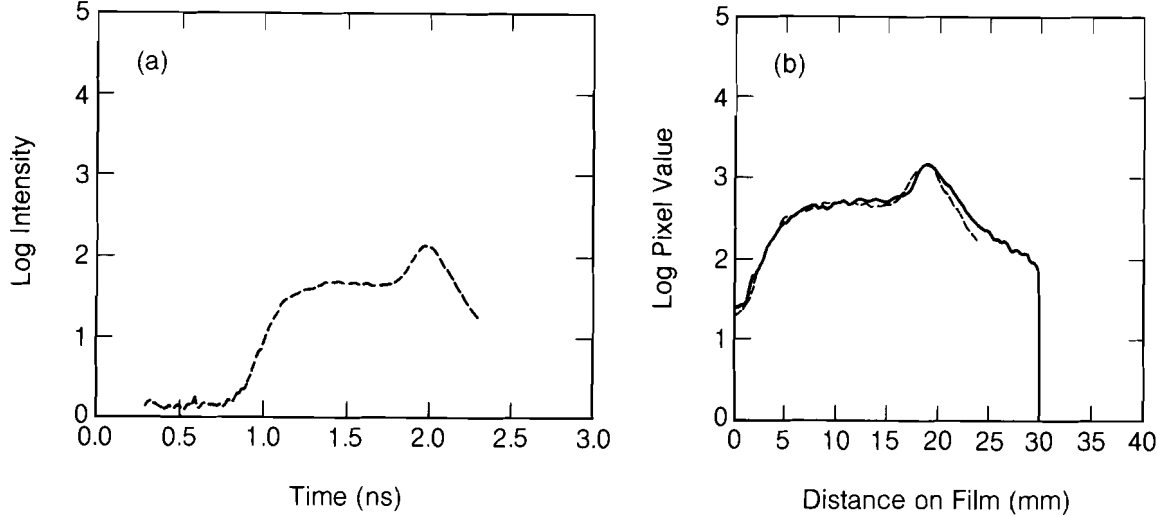
program written in Magic/L calculates the center of a pinhole picture and the image is then azimuthally averaged. This gives a plot of intensity as a function of radius, which can be compared with the one-dimensional results from the *LILAC* hydrocode for similar experimental conditions.⁴

Two x-ray microscopes and a pinhole camera are also used to determine the pointing and focusing accuracy of the OMEGA laser. Figure 28.33, which was previously discussed, shows a contour-plotted and shaded hemispheric view of a metal target used for pointing. Precalculated circles of idealized beam positions (which project as ellipses onto a flat plane) are superimposed over the data. This image indicates that the OMEGA laser was very well pointed for this shot. In the event that a beam was mispointed, that is, pointed outside the calculated beam position, the hard-copy image can be directly measured and appropriate corrections made.

A common method of interpreting spectra is to take a series of lineouts, as shown in Fig. 28.36(a). A typical time-resolved x-ray emission of narrow spectral band around 2.46 keV, obtained with the SPEAXS instrument, is plotted here as log(intensity) versus time. The highest peak at 2 ns indicates peak compression of the target. An absolute time scale is possible for this diagnostic through the use of optical timing fiducials.⁵ The solid line in Fig. 28.36(b) is from an x-ray transmission-grating streak camera, where the log of the intensity is plotted as a function of position on film; no direct time calibration is available. However, comparison with a lineout from the timed SPEAXS diagnostic [from Fig. 28.36(a)] enables cross-calibration of the timing of the transmission-grating streak camera.

Fig. 28.36

- (a) X-ray time-resolved spectrum obtained on SPEAXS.
- (b) X-ray transmission-grating streak camera lineout compared with the corresponding SPEAXS result.



Conclusion

The majority of the effort to date has gone toward developing an accurate representation of intensity values from film densities for IR, visible, UV, and x-ray films. Additional effort has resulted in a flexible system responding to needs of routine users, through menu-driven software, and enabling users to write specialized image processing codes.

ACKNOWLEDGMENT

This work was supported by the U.S. Department of Energy Office of Inertial Fusion under agreement No. DE-FC08-85DP40200 and by the Laser Fusion Feasibility Project at the Laboratory for Laser Energetics, which has the following sponsors: Empire State Electric Energy Research Corporation, General Electric Company, New York State Energy Research and Development Authority, Ontario Hydro, Southern California Edison Company, and the University of Rochester. Such support does not imply endorsement of the content by any of the above parties.

REFERENCES

1. B. Courington, "The UNIX System: A Sun Technical Report," Sun Microsystems (1985).
2. B. L. Henke *et al.*, *J. Opt. Soc. Am. B*, **1**, 818 (1984).
3. LLE Review **23**, 104 (1985).
4. G. G. Gregory, S. A. Letzring, and M. C. Richardson, *Bull. Am. Phys. Soc.* **30**, 1481 (1985).
5. P. A. Jaanmagi, L. DaSilva, G. G. Gregory, C. Hestdalen, C. D. Kiikka, R. Kotmel, and M. C. Richardson, *Rev. Sci. Inst.* **57**, 2189 (1986).

Section 4

NATIONAL LASER USERS FACILITY NEWS

National Laser Users Facility (NLUF) activity during the fourth quarter of FY86 supported the experiments of **Dr. J. G. Jernigan** from the Space Sciences Laboratory at the University of California, Berkeley; **Professor C. F. Hooper** from the University of Florida; **Dr. T. R. Fisher** from the Lockheed Palo Alto Research Laboratory; and **Professor C. J. Joshi** from the University of California, Los Angeles. The experiments of Dr. Jernigan, Dr. Fisher, and Professor Joshi are in the initial stages of setup and experimental review. Professor Hooper visited the NLUF to review data collected during FY86 experiments.

Dr. Jernigan is collaborating with **Dr. F. Marshall** of LLE on the development of a two-dimensional PIN diode array that can be used with x-ray detectors. The objective is to place this array on LLE's 8-in. pinhole camera to get an image of a radiating target. The PIN diode array has 10×64 elements, with a $120\text{-}\mu\text{m} \times 120\text{-}\mu\text{m}$ pixel size. The array has arrived from the University of California, Berkeley. During this quarter, the interface electronics has been connected via Ethernet to the LLE image-processing system. The PIN diode array has been tested with a dc x-ray source to make sure that it was not damaged in shipment. The apparatus is now ready to mount on the pinhole camera and be installed on the OMEGA target tank.

Professor Hooper carried out spectroscopic studies of targets with krypton mixed with the deuterium-tritium. X-ray lines have been identified for Kr XVIII – Kr XXIV transitions from time-integrated x-ray spectra.

Time-integrated, spatially resolved spectra were shown by Dr. P. **Audebert** of LLE and will be used by the University of Florida researchers in their analysis. Time-resolved data from the SPEAXS spectrometer (developed by Dr. P. **Jaanimagi** of LLE and Professor B. L. **Henke** of Lawrence Berkeley Laboratory) were presented by Dr. Jaanimagi. All of this data will be used to develop diagnostic methods to measure the temperature and density of imploded target cores.

Dr. Fisher visited LLE for an experimental design review of the supersonic gas-jet experiment. The jet has been characterized by Lockheed scientists and has been shown to be a Mach-6 jet with a peak density of 2×10^{18} atoms/cm³. This is by a factor of 5 less than the value 10^{19} atoms/cm³ stated in the proposal, but was shown to be sufficient to get the time-dependent data desired. Initial laser-heating experiments have been done at Lockheed with a neon gas. Spectral lines from Ne V - Ne VIII appeared in the x-ray spectrum. Dr. Fisher also showed data taken with a strip-line x-ray diode array fitted to the Rowland circle of a grazing-incidence spectrograph. Signal levels were in the range of 5 mV-20 mV. Some tests of the OMEGA target chamber environment need to be made so that these small signals can be recorded.

Professor Joshi has received funding for his self-focusing and filamentation instability experiment on GDL. Sketches of the GDL target chamber and current GDL parameters were sent to him for the design of the experiment. When this is completed, a design review will be held at LLE.

Proposals for consideration for the FY88 funding cycle are due by 15 December 1986.

For more information regarding proposal guidelines and the resources available at the National Laser Users Facility, please contact:

Manager
National Laser Users Facility
Laboratory for Laser Energetics
University of Rochester
250 East River Road
Rochester, New York 14623-1299
(716) 275-2074

ACKNOWLEDGMENT

This work was supported by the U.S. Department of Energy Office of Inertial Fusion under agreement No. DE-FC08-85DP40200.

PUBLICATIONS AND CONFERENCE PRESENTATIONS

Publications

- B. Yaakobi, O. Barnouin, M. C. Richardson, J. M. Soures, A. Hauer, and B. Post, "X-Ray Spectroscopic Methods for the Diagnosis of Laser-Imploded Targets," *Rev. Sci. Instrum.* **57**, 2124–2128 (1986).
- P. A. Jaanimagi, L. DaSilva, G. G. Gregory, C. Hestdalen, C. D. Kiikka, R. Kotmel, and M. C. Richardson, "Optical Fiducials for X-Ray Streak Cameras at LLE," *Rev. Sci. Instrum.* **57**, 2189–2191 (1986).
- M. C. Richardson, R. F. Keck, S. A. Letzring, R. L. McCrory, P. W. McKenty, D. M. Roback, J. M. Soures, C. P. Verdon, S. M. Lane, and S. G. Prussin, "Neutron Diagnosis of Compressed ICF Targets," *Rev. Sci. Instrum.* **57**, 1737–1739 (1986).
- J. S. Wark, A. Hauer, and J. D. Kilkenny, "Studies of X-Ray Switching and Shuttering Techniques," *Rev. Sci. Instrum.* **57**, 2168–2170 (1986).
- P. G. Burkhalter, D. A. Newman, D. L. Rosen, K. Hudson, M. C. Richardson, and P. Audebert, "Spectral Measurements from Laser-Produced Plasma in OMEGA," *Rev. Sci. Instrum.* **57**, 2171–2173 (1986).
- S. G. Prussin, S. M. Lane, M. C. Richardson, and S. G. Noyes, "Debris Collection from Implosion of Microballoons," *Rev. Sci. Instrum.* **57**, 1734–1736 (1986).
- S. M. Lane, M. D. Cable, S. G. Prussin, S. G. Glendinning, D. H. Munro, S. P. Hatchett, K. G. Estabrook, L. J. Suter, and M. C. Richardson, "High-Yield Direct Drive Experiments at NOVA," *Rev. Sci. Instrum.* **57**, 2100 (1986).

- P. A. Jaanimagi, J. Delettrez, B. L. Henke, and M. C. Richardson, "Temporal Dependence of the Mass-Ablation Rate in UV-Laser-Irradiated Spherical Targets," *Phys. Rev. A* **34**, 1322–1327 (1986).
- A. Hauer, R. D. Cowan, B. Yaakobi, O. Barnouin, and R. Epstein, "Absorption-Spectroscopy Diagnosis of Pusher Conditions in Laser-Driven Implosions," *Phys. Rev. A* **34**, 411–420 (1986).
- R. S. Craxton, R. L. McCrory, and J. M. Soures, "Progress in Laser Fusion," *Scientific American* **255**, 68–79 (1986).
- S. D. Jacobs, "Liquid Crystal Devices for Laser Systems," *J. Fusion Energy* **5**, 65–75 (1986).
- J. Nees and G. Mourou, "Noncontact Electro-Optic Sampling with a GaAs Injection Laser," *Electron. Lett.* **22**, 918–919 (1986).
- J. F. Whitaker and G. A. Mourou, "Optical Reconfiguration of Electrical Networks," *Electron. Lett.* **22**, 899–900 (1986).
- B. Yaakobi, R. D. Frankel, J. M. Forsyth, and J. M. Soures, "Laser-Generated X-Ray Source for Time-Resolved Biological and Material Structure Studies," *Structural Biological Applications of X-Ray Absorption, Scattering, and Diffraction* (Academic Press, San Diego, CA, 1986), pp. 331–348.
- A. Simon, "Raman Scattering," *Can. J. Phys.* **64**, 956–960 (1986).
- L. M. Goldman, W. Seka, K. Tanaka, R. Short, and A. Simon, "The Use of Laser Harmonic Spectroscopy as a Target Diagnostic," *Can. J. Phys.* **64**, 969–976 (1986).
- J. Delettrez, "Thermal Electron Transport in Direct-Drive ICF," *Can. J. Phys.* **64**, 932–943 (1986).
- S. D. Jacobs, "Liquid Crystals for Laser Applications," in *Handbook of Laser Science and Technology*, edited by M. J. Weber (CRC Press, Boca Raton, FL, 1986), Vol. IV, Part 2, pp. 409–465.

Forthcoming Publications

The following papers are to be published in the *Proceedings of the 17th Annual Boulder Damage Symposium*, Boulder, CO, October 1985:

- K. A. Cerqua, S. D. Jacobs, B. L. McIntyre, and W. Zhong, "Ion Exchange Strengthening of Nd-Doped Phosphate Laser Glass."
- B. Liao, D. J. Smith, and B. L. McIntyre, "The Development of Nodular Defects in Optical Coatings."
- D. J. Smith, B. Krakauer, C. J. Hayden, A. W. Schmid, and M. J. Guardalben, "Yttrium-Oxide-Based Anti-Reflection Coating for High Power Lasers at 351 nm."

The following articles are to be published in *Laser Interaction and Related Plasma Phenomena* Vol. 7, edited by G. Miley and H. Hora (Plenum Press, New York, in press):

M. C. Richardson, P. W. McKenty, F. J. Marshall, C. P. Verdon, J. M. Soures, R. L. McCrory, O. Barnouin, R. S. Craxton, J. Delettrez, R. L. Hutchison, P. A. Jaanimagi, R. Keck, T. Kessler, H. Kim, S. A. Letzring, D. M. Roback, W. Seka, S. Skupsky, B. Yaakobi, and S. M. Lane, "Ablatively Driven Targets Imploded with the 24 UV Beam OMEGA System."

M. C. Richardson, G. G. Gregory, R. L. Keck, S. A. Letzring, R. S. Marjoribanks, F. J. Marshall, G. Pien, J. S. Wark, B. Yaakobi, J. D. Goldstone, A. Hauer, G. S. Stradling, F. Ameduri, B. L. Henke, and P. A. Jaanimagi, "Time-Resolved X-Ray Diagnostics for High Density Plasma Physics Studies."

B. Yaakobi, O. Barnouin, C. B. Collins, R. Epstein, A. Hauer, S. A. Letzring, F. J. Marshall, R. L. McCrory, M. C. Richardson, J. M. Soures, and S. Wagel, "Laser-Generated X-Ray Studies Relevant to Compression Diagnostics and Nuclear Level Excitation."

W. C. Mead, S. V. Coggeshall, S. R. Goldman, E. K. Stover, P. D. Goldstone, A. Hauer, V. M. Kindel, L. Montierth, M. C. Richardson, O. Barnouin, P. A. Jaanimagi, R. S. Marjoribanks, R. L. Kauffman, H. Kornblum, and B. F. Lasinski, "Analysis, Modeling, and Design of Short Wavelength Laser Plasma Experiments."

B. Yaakobi, "X-Ray Diagnostic Methods for Laser-Imploded Targets" and "Thermal Transport, Mass Ablation, and Preheat in Laser-Target Experiments," to be published in the *Proceedings of the Spring College on Radiation in Plasmas*, Trieste, Italy, June 1985 (World Scientific Publishing Co.).

G. Pien, M. C. Richardson, P. D. Goldstone, R. H. Day, F. Ameduri, and G. Eden, "Computerized 3-GHz Multichannel Soft X-Ray Diode Spectrometer for High-Density Plasma Diagnosis," to be published in *Nuclear Instruments and Methods*.

S. D. Jacobs, A. L. Hrycin, K. A. Cerqua, C. Kennemore III, and U. Gibson, "Adhesion Enhancements and Internal Stress in MgF₂ Films Deposited with an Ion Beam Assist," to be published in the *Journal of Thin Solid Films*.

The following articles are to be published in the *Journal of the Optical Society of America B*:

U. Feldman, J. F. Seely, C. M. Brown, J. D. Ekberg, M. C. Richardson, W. E. Behring, and J. Reader, "Spectrum and Energy Levels of Br XXV, Br XXIX, Br XXX, and Br XXXI."

W. E. Behring, C. M. Brown, U. Feldman, J. F. Seely, J. Reader, and M. C. Richardson, "Transitions of the Type 2s-2p in Oxygenlike Y, Zr, and Nb."

P. A. Holstein, J. Delettrez, S. Skupsky, and J. P. Matte, "Modeling Nonlocal Heat Flow in Laser-Produced Plasmas," to be published in the *Journal of Applied Physics*.

J. F. Whitaker, T. Norris, G. A. Mourou, and T. Y. Hsiang, "Pulse Dispersion and Shaping in Microstrip Lines," to be published in *IEEE Microwave Theory and Techniques Society Transactions*.

M. C. Richardson, B. Yaakobi, R. Epstein, J. Wark, and J. M. Soures, "Imploding Cylindrical Plasmas as X-Ray Laser Media," to be published in the *Proceedings of the 1986 Quebec International Symposium on Optical and Optoelectronic Applied Sciences and Engineering*, Quebec City, June 1986.

S. H. Batha and C. J. McKinstry, "Energy Cascading in the Beat-Wave Accelerator," to be published in a special issue of *IEEE Transactions on Plasma Science on Plasma-Based High-Energy Accelerators*.

D. R. Dykaar, R. Sobolewski, T. Y. Hsiang, and G. A. Mourou, "Response of a Josephson Junction to a Stepped Voltage Pulse," to be published in *IEEE Transactions on Magnetics*.

J. M. Soures, R. L. McCrory, K. A. Cerqua, R. S. Craxton, R. Hutchison, S. D. Jacobs, T. J. Kessler, J. Kelly, G. Mourou, W. Seka, and D. Strickland, "High Power Laser Research and Development at the Laboratory for Laser Energetics," to be published in the *Proceedings of SPIE's Fiber LASE Applications in Science and Engineering '86 Symposium*, Cambridge, MA, September 1986.

H. L. Helfer and R. L. McCrory, "Some Properties of a Polarized OCP," to be published in *Strongly Coupled Plasmas*, edited by Forest Rogers and Hugh DeWitt (Plenum Press, New York).

J. F. Whitaker and G. A. Mourou, "Optical Reconfiguration of Electrical Networks," to be published in *Electronics Letters*.

G. Mourou, "Picosecond Electro-Optic Sampling," to be published in the *Proceedings of the High Speed Electronics Conference*, Stockholm, Sweden, August 1986.

Conference Presentations

The following presentations were made at the 16th Annual Anomalous Absorption Conference, Lake Luzerne, NY, July 1986:

P. A. Jaanimagi, L. DaSilva, J. Delettrez, G. G. Gregory, and M. C. Richardson, "Time-Resolved Absorption Measurements on OMEGA."

P. Audebert, O. Barnouin, J. Delettrez, F. J. Marshall, and B. Yaakobi, "Space-Resolved X-Ray Spectra of Imploding Laser Fusion Targets."

S. H. Batha, L. M. Goldman, W. Seka, and A. Simon, "Raman Scattering from Inhomogeneous Plasmas."

R. S. Craxton and R. L. McCrory, "Thermal Self-Focusing with Multiple Beams."

J. Delettrez, R. Epstein, P. A. Jaanimagi, T. J. Kessler, M. C. Richardson, W. Seka, and S. Skupsky, "Effects of Illumination Non-Uniformities on the Interpretation of Spherical Transport Experiments."

R. Epstein, J. Delettrez, and S. Skupsky, "Non-LTE Radiation and Ion-Dynamic Effects in Hydrodynamic Simulations of Laser-Driven Plasmas."

F. J. Marshall, L. G. DaSilva, G. G. Gregory, S. A. Letzring, R. L. McCrory, P. W. McKenty, M. C. Richardson, J. M. Soures, C. P. Verdon, and J. S. Wark, "Results of Short-Pulse UV-Driven High-Aspect-Ratio Implosion Experiments on the University of Rochester OMEGA Laser System."

R. W. Short, "Stimulated Raman Scattering in Filaments."

A. Simon, R. W. Short, K. Swartz, and W. Seka, "Raman Scattering Via Enhanced Thomson: Further Studies."

K. Swartz, R. W. Short, and A. Simon, "Raman Scattering Driven by Multiple Pumps in Laser Fusion Plasmas."

J. S. Wark, S. A. Letzring, F. J. Marshall, R. L. McCrory, M. C. Richardson, J. M. Soures, C. P. Verdon, and J. Delettrez, "Alpha Particle Imaging of High-Yield Implosions."

M. C. Richardson, L. DaSilva, G. G. Gregory, P. A. Jaanimagi, S. A. Letzring, F. J. Marshall, R. L. McCrory, P. W. McKenty, D. M. Roback, J. M. Soures, C. P. Verdon, and J. S. Wark, "Implosion Dynamics of Low-Aspect-Ratio Gas-Filled Targets Driven by UV Radiation."

L. DaSilva, P. A. Jaanimagi, J. Delettrez, R. Epstein, G. G. Gregory, and M. C. Richardson, "Time-Resolved Ablation Measurements of Imploding Targets."

C. J. McKinstry, D. W. Forslund, and S. H. Batha, "Nonlinear Stimulated Raman Scattering in the Beat Wave Accelerator."

The following presentations were made at SPIE's 30th Annual International Technical Symposium, San Diego, California, August 1986:

S. D. Jacobs, J. E. Hayden, and A. L. Hrycin, "Practical Measurements of Adhesion and Strain for Improved Optical Coatings."

R. S. Marjoribanks, P. A. Jaanimagi, and M. C. Richardson, "Principles of Streak and Framing Photography by Optical Frequency-Encoding on a Chirped Pulse."

G. A. Mourou, "Picosecond Electro-Optic Sampling," presented at the High Speed Electronics Conference, Stockholm, Sweden, August 1986.

D. R. Dykaar, R. Sobolewski, T. Y. Hsiang, and G. A. Mourou, "Response of a Josephson Junction to a Stepped Voltage Pulse," presented at the 1986 Applied Super-Conductivity Conference, Baltimore, MD, September/October 1986.

J. M. Soures, R. L. McCrory, K. A. Cerqua, R. S. Craxton, R. J. Hutchison, S. D. Jacobs, T. J. Kessler, J. Kelly, G. A. Mourou, W. Seka, and D. Strickland, "High Power Laser Research and Development at the Laboratory for Laser Energetics," presented at SPIE's Fiber LASE Applications in Science and Engineering '86 Symposium, Cambridge, MA, September, 1986.

ACKNOWLEDGMENT

The work described in this volume includes current research at the Laboratory for Laser Energetics, which is supported by Empire State Electric Energy Research Corporation, General Electric Company, New York State Energy Research and Development Authority, Ontario Hydro, Southern California Edison Company, the University of Rochester, and the U.S. Department of Energy Office of Inertial Fusion under agreement No. DE-FC08-85DP40200.